

## James Webb Space Telescope optical stability lessons learned for future great observatories

Lee D. Feinberg,<sup>a,\*</sup> Michael W. McElwain,<sup>b</sup> Charles W. Bowers,<sup>a</sup> John D. Johnston,<sup>b</sup> Gary E. Mosier,<sup>a</sup> Randy A. Kimble,<sup>a</sup> Joshua S. Levi,<sup>b</sup> Paul Lightsey,<sup>c</sup> J. Scott Knight,<sup>c</sup> Marcel Bluth,<sup>d</sup> Alden S. Jurling,<sup>a</sup> Marie B. Levine,<sup>e</sup> D. Scott Acton,<sup>c</sup> Charles Atkinson,<sup>b</sup> Allison Barto,<sup>c</sup> Matthew D. Bergkoetter,<sup>a</sup> Gregory R. Brady,<sup>f</sup> Larkin Carey,<sup>c</sup> Lester Cohen,<sup>g</sup> Laura Coyle,<sup>c</sup> Bruce H. Dean,<sup>a</sup> Michael Eisenhower,<sup>b</sup> Nicolas Flagey,<sup>f</sup> George F. Hartig,<sup>f</sup> Keith A. Havey,<sup>h</sup> Brian Hicks,<sup>b</sup> Joseph M. Howard,<sup>a</sup> Ritva A. Keski-Kuha,<sup>a</sup> Charles-Philippe Lajoie,<sup>f</sup> Matthew D. Lallo,<sup>f</sup> Gary W. Matthews,<sup>i</sup> Marcio Meléndez,<sup>f</sup> Michael T. Menzel,<sup>a</sup> Sang Park,<sup>g</sup> Marshall D. Perrin,<sup>f</sup> Laurent Pueyo,<sup>f</sup> Lisbeth Quesnel,<sup>h</sup> Paul Reynolds,<sup>b</sup> Jane R. Rigby,<sup>a</sup> Babak N. Saif,<sup>a</sup> Christopher C. Stark,<sup>a</sup> Randal Telfer,<sup>f</sup> Scott C. Texter,<sup>b</sup> Julie M. Van Campen,<sup>a</sup> Begoña Vila,<sup>j</sup> Garrett West,<sup>c</sup> Erin Wolf,<sup>c</sup> Tony L. Whitman,<sup>h</sup> and Thomas P. Zielinski<sup>a</sup>

<sup>a</sup>Goddard Space Flight Center, Greenbelt, Maryland, United States

<sup>b</sup>Northrop Grumman Space Systems, Redondo Beach, California, United States

<sup>c</sup>Ball Aerospace, Boulder, Colorado, United States

<sup>d</sup>Intuitive Machines, LLC, Houston, Texas, United States

<sup>e</sup>Jet Propulsion Laboratory, Pasadena, California, United States

<sup>f</sup>Space Telescope Science Institute, Baltimore, Maryland, United States

<sup>g</sup>Smithsonian Astrophysical Observatory, Cambridge, Massachusetts, United States

<sup>h</sup>L3Harris Corporation, Rochester, New York, United States

<sup>i</sup>Aerodyne Industries, Cape Canaveral, Florida, United States

<sup>j</sup>KBR, Aberdeen, Maryland, United States

**ABSTRACT.** The James Webb Space Telescope (JWST) launched on December 25, 2021, and its optical performance in orbit has been even better than predicted pre-flight. The static wavefront error (WFE) is less than half the value specified for the requirement of having diffraction-limited image quality at 2 microns in the NIRCам shortwave channel, enabling the observatory to deliver both sharper images and higher sensitivity than anticipated. In addition to the excellent image quality, the optical stability has also exceeded expectations, both in terms of high-frequency dynamic contributions (which would be perceived as part of “static WFE”) and in terms of drifts over minutes, hours, and days. Stability over long timescales is critical for several important science cases, including exoplanet transit spectroscopy and coronagraphy. JWST’s stability success was achieved through detailed design and testing, with several important lessons learned for future observatories, especially the Habitable Worlds Observatory that is expected to need even higher levels of stability. We review the stability architecture, how it was technologically demonstrated, the ground test results and improvements, the on-orbit results, and the lessons learned.

© The Authors. Published by SPIE under a Creative Commons Attribution 4.0 International License. Distribution or reproduction of this work in whole or in part requires full attribution of the original publication, including its DOI. [DOI: [10.1117/1.JATIS.10.1.011204](https://doi.org/10.1117/1.JATIS.10.1.011204)]

**Keywords:** James Webb Space Telescope; infrared space telescopes; integration and testing; observatories

Paper 23058SS received May 17, 2023; revised Aug. 21, 2023; accepted Oct. 3, 2023; published Nov. 15, 2023.

\*Address all correspondence to Lee D. Feinberg, [lee.d.feinberg@nasa.gov](mailto:lee.d.feinberg@nasa.gov)

## 1 Introduction

After a year in orbit, both the static wavefront error (WFE) and the stability of the James Webb Space Telescope (JWST) are well known and both are either meeting or exceeding expectations in every aspect.<sup>1,2</sup> The wavefront sensing and control team uses a well-defined process to correct the active primary mirror (PM) (with its 18 separate segments, controllable in six degrees of freedom and radius of curvature) when the full observatory static wavefront rises to 70 nm RMS at the NIRCcam control field point, making this the upper bound of static performance, better than two times the tightest specification in any instrument channel of 150 nm RMS.

In this paper, we discuss JWST stability starting with the driving requirements in Sec. 2. Section 3 discusses the dynamics, jitter, and line of sight (LOS) by providing an overall summary of how it was modeled and validated. This is followed by Sec. 4, which covers thermal stability starting with the approach to designing the overall athermal architecture and backplane and then discussing the testing including several critical workmanship findings during the test program. Section 5 covers tilt events that were seen during testing at NASA's Johnson Space Center (JSC) and initially on-orbit. While lessons learned are included at the end of individual sections, Sec. 6 concludes the paper with a final set of summary lessons learned.

While the static wavefront was a major accomplishment, in many ways the stability performance was an even more challenging task, due to the passive nature, size, mass, and temperature of the telescope, and the way this requirement cut across so many systems from dynamics and pointing to thermal stability. JWST had a significant amount of soft structure ranging from cables to insulation to tape and lacing cord, which all presented complications for a cryogenic system with tight stability requirements. Given these challenges and reliance on so much soft structure, stability was the area where the ground test program caught workmanship issues that needed actual hardware and operational improvements. Several repairs were undertaken as a result of the ground test and inspection findings. In the end, a key lesson learned from the stability effort was the importance of the ground test program to catch workmanship-related issues that could have been missed.

While the passive architecture (where passive is defined as updating the PM on the order of days, not seconds or minutes) was determined to be the best design for a cryogenic telescope of this mass, its complex verification, which was not fully understood early on is an overarching lesson learned: considering the verification approach while designing the architecture is important and active methods of control can make verification simpler and less complex. The next great observatory, the Habitable Worlds Observatory, has even tighter stability specifications, so understanding the successes and the lessons learned from JWST and applying them early even in the architecture phase is critical so that stability verification will be successful and low risk.

## 2 Driving Requirements

The science objectives for JWST drive the optical performance to have a point spread function (PSF) that provides the desired diffraction-limited image quality and angular resolution. The optical performance was specified using the Strehl ratio metric, which was converted to WFE for the optical error budget. In addition, the science objectives drive requirements for photometric stability; the photometric stability allocation was specified in terms of the stability of the encircled energy (EE) within an angular photometric aperture (i.e., the stability of the EE within an 80 mas radius aperture at a wavelength of 2  $\mu\text{m}$ ).<sup>3</sup> The EE requirement was in turn converted into allocations of WFE stability. The stability of the EE with respect to WFE depends on the nature of the spatial frequency content to the WFE. The allocation for global WFE tilt, which is equivalent to LOS motion, was sufficiently small such that changes between zero and maximum allowable (<7 mas RMS LOS) has no impact on the EE, but LOS motion is an important component included in the total WFE budget for image quality. Thus, the WFE allocation for stability was tracked in terms of the higher order low, mid, and high spatial content of the WFE. The allocations were apportioned between surface figure and alignment effects at the top level. The surface figure and alignment allocations were further partitioned between the phenomena affecting stability; specifically, thermal distortion effects and vibrational response to dynamic

disturbances. Note that response to steady state disturbances such as the cryo-cooler compressor running at constant speed are not included in the stability budget but are part of the “static” budget for overall image quality.

## 2.1 Wavefront Error Budget

As discussed, the system stability of JWST was defined through a detailed error budget that flowed from key performance requirements to system level optical requirements and down to stability terms (see Fig. 1). The top level 150 nm RMS WFE requirement through the NIRCcam short wavelength channel allocates 122 nm RMS for the optical telescope element (OTE) component. The rest is primarily the NIRCcam instrument itself. The OTE budget further breaks down between image motion equivalent, which relates to the top level image motion requirement, the OTE stability along with steady state and wavefront control residuals. The emphasis of this paper will be on the OTE stability and image motion portions of the allocations. The top level OTE stability is given an allocation of 57 nm RMS WFE (system is 59 nm RMS), an important component of the total 150 nm RMS WFE requirement. The 57 nm is further decomposed into low, mid, and high spatial frequency where mid spatial frequencies are defined as above the control frequency of above 5 cycles per aperture and high spatial frequencies are higher than 30 cycles per aperture. For each term in the budget there is a requirement (or allocation) value assigned, a predicted plus uncertainty (P + U) value, and the individual predicted and uncertainty values. Details of how the predicted plus uncertainty value is calculated is dependent on whether the uncertainties are correlated or uncorrelated. Below the overall

| nm    | OTE totals |    |     |    |
|-------|------------|----|-----|----|
| RMS   | tot        | lo | mid | hi |
| Alloc | 122        | 92 | 74  | 30 |
| P+U   | 115        | 83 | 71  | 37 |
| pred  | 81         | 53 | 55  | 26 |
| unc   | 74         | 59 | 37  | 26 |

| nm   | OTE WFC residual |    |     |    |
|------|------------------|----|-----|----|
| RMS  | tot              | lo | mid | hi |
| Req  | 81               | 41 | 63  | 30 |
| P+U  | 78               | 33 | 60  | 37 |
| pred | 60               | 21 | 50  | 26 |
| unc  | 51               | 29 | 34  | 26 |

| nm    | OTE stability |    |     |    |
|-------|---------------|----|-----|----|
| RMS   | tot           | lo | mid | hi |
| Alloc | 57            | 43 | 38  | 0  |
| P+U   | 54            | 40 | 36  | 0  |
| pred  | 34            | 25 | 22  | 0  |
| unc   | 21            | 15 | 14  | 0  |

| nm    | OTE steady state vbe |    |     |    |
|-------|----------------------|----|-----|----|
| RMS   | tot                  | lo | mid | hi |
| Alloc | 13                   | 11 | 7   | 0  |
| P+U   | 7                    | 0  | 7   | 0  |
| pred  | 3                    | 0  | 3   | 0  |
| unc   | 3                    | 0  | 3   | 0  |

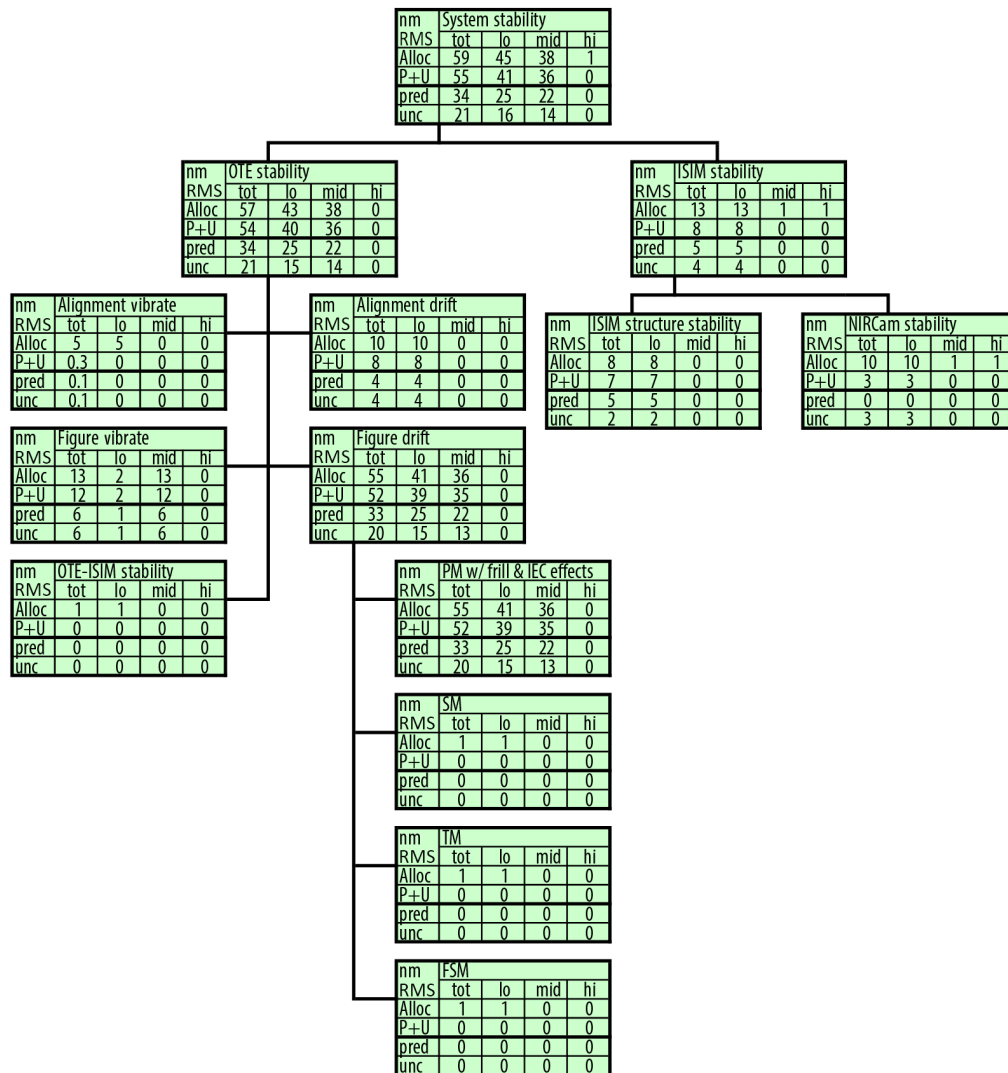
  

| nm   | Image motion equ. |         |     |    |
|------|-------------------|---------|-----|----|
| RMS  | tot               | lo      | mid | hi |
| Req  | 69                | 69      | 0   | 0  |
| P+U  | 64                | 64      | 0   | 0  |
| pred | 41                | 41      | 0   | 0  |
| unc  | 49                | 49      | 0   | 0  |
| Req  | los               | 6.2 mas |     |    |
| P+U  | los               | 5.7 mas |     |    |
| pred | los               | 3.7 mas |     |    |
| unc  | los               | 4.3 mas |     |    |

**Fig. 1** The top-level OTE WFE budget has contributions from image motion, OTE stability, OTE steady state vibration, and wavefront control residuals. For each term, there are values for the requirement or allocation, predicted plus uncertainty, and the separate predicted and uncertainty values. Details of the predicted plus uncertainty calculation are dependent on whether the uncertainties are correlated or uncorrelated.

system stability is the allocation to the OTE and integrated science instrument module (ISIM) (see Fig. 2). The ISIM is composed of the structure stability and the instrument itself (in this case NIRCam). The instrument allocations are small and can essentially be ignored for this discussion.

The OTE portion of the stability budget has five major areas. The first two are alignment vibrate and drift. The vibrate portion covers jitter and high frequency changes while the drift covers slow changes such as thermal. Alignment covers the motions of mirrors in rigid-body; a key piece of this is the secondary mirror (SM) alignment, which affects the LOS. The other key areas are the figure vibrate and drift, which impact the wavefront of the PM itself. The figure drift was a key area where workmanship issues could arise because the large PM interfaces to the optomechanical structure, including different forms of soft structure that could induce strain. This includes cables and harnesses, insolation, and the “frill,” which is black Kapton surrounding the PM for stray light management [see Sec. 4.4 PM long term drift instability (CoCOA-measurement and frill-induced)]. Cyclic heater behavior [e.g., the ISIM electronics compartment (IEC) heaters) would fall under drift and could impact soft structures that change the figure drift on the scale of seconds and minutes [see Sec. 4.4.4 cyclic optical instability (IEC heater-induced oscillations)]. The error budget also includes the OTE-ISIM interface although this allocation was designed to be a small portion of the budget.



**Fig. 2** Stability error budget/requirements: top level system stability in nanometers RMS consists of OTE and ISIM stability. Dominant contributors are predicted to be IEC heater oscillation and Frill effects.

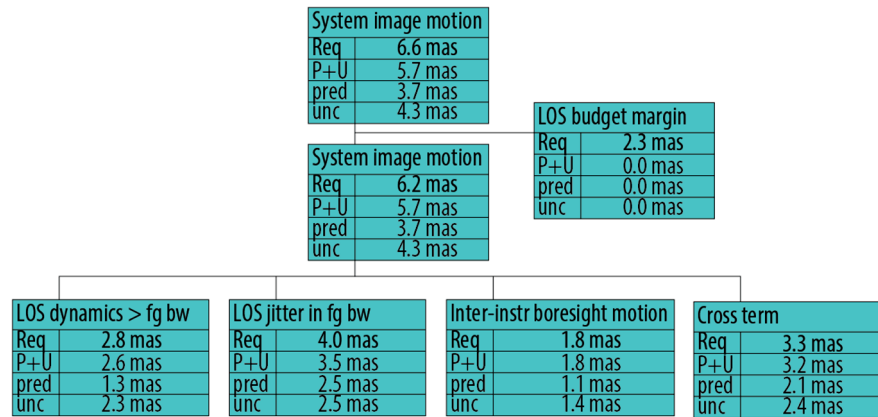


**Fig. 3** The LOS error budget sets an image motion requirement in milliarcseconds over a 10,000 second interval. This image motion is allocated to dynamics above the fine guidance bandwidth, the jitter in the fine guidance bandwidth, inter-science instrument boresight motion, and a cross term. The image motion in milliarcseconds was converted to a nanometers RMS of WFE equivalent in the WFE budget.

The image motion portion of the budget is primarily driven by the LOS stability, as shown in Fig. 3. Note that the LOS budget is driven primarily by the LOS jitter and dynamics including the fine guide sensor.

### 3 Line-of-Sight, Dynamics, and Attitude Control

The stability of the observatory is primarily driven by two key factors. First is dynamics, which is higher frequency and impact LOS motion and high frequency changes to the PM. The second factor is thermal distortion stability, which will be discussed later. In this section, we will discuss dynamics and LOS motion, which is partially corrected by a fine steering mirror (FSM) control loop.

Jitter refers to the contributors to LOS stability, or image motion, that occur at frequencies above the 0.5 Hz bandwidth of the fine guidance sensor (FGS)-FSM control loop that was designed to attenuate low-frequency errors including thermal drift and attitude control system (ACS) sensor noise. For JWST, we extend this definition to include dynamic contributions to WFE. The two primary dynamic disturbance sources, which contribute to both LOS and WFE, are the reaction wheels and the MIRI cryocooler. Other potential disturbances, such as fuel slosh, the high gain antenna, instrument mechanisms, thrusters, and micro-dynamic stick/slip events, were not modeled for purposes of the jitter predictions. The thrusters and mechanisms do not operate during exposures, and stick/slip events are rare, unpredictable in terms of location and intensity, and the transient effects dissipate quickly.

The LOS predictions from the jitter analysis are one of the three main components of the image motion budget that fall within the scope of observatory systems “integrated modeling.” The two others are the roll stability predictions from the thermal distortion analysis and the three-axis pointing stability predictions from the ACS fine pointing performance analysis.

#### 3.1 Architecture

Several layers of architectural features were implemented on the telescope to control the image motion. The image motion contributors are “smear” with non-zero mean motion and “jitter” with zero mean motion over an image collection. Jitter derives from dynamic sources and smear derives from thermal distortion and very low frequency disturbances. Of course, in addition to the telescope architectural features, high quality components with low exported forces and moments were chosen for the bus. For example, the cryocooler and reaction wheels have isolation from the bus structure.

The primary architecture element to combat image motion relies on an active FSM. This system measures image motion in two translation axes in the FGS by measuring the image centroid of a star relative to the desired guide star with 16 Hz cadence. The FGS signal is processed

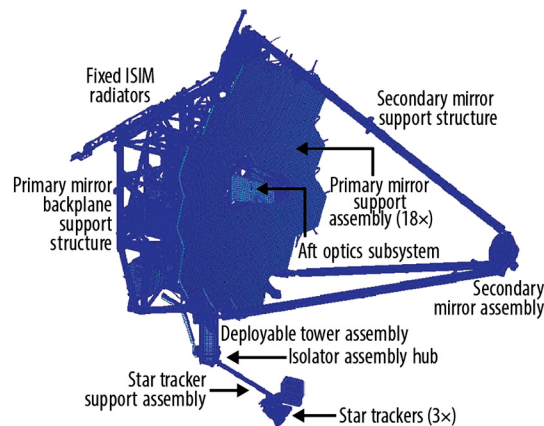


**Fig. 4** The thermal distortion finite element model (FEM) of the deployed observatory illustrates the mechanical interface between the OTE and the star tracker. Connecting these mechanically mitigates smear despite a long lever arm and temperature differences between them.

by the fine guidance control (FGC) loop and feedback to the FSM at 16 Hz with a control bandwidth of 0.78 Hz. Since roll about the guide star cannot be measured (with a single star), roll of the field of view (FOV) is controlled using the star trackers and ACS. This system works to control dynamic image motion in each instrument since the dominant contributors are common to all instruments. The fine guidance and ACS provide image motion disturbance rejection for low frequencies. The non-common-path dynamic motion was very small due to the structural design and the small optical LOS sensitivities in the instruments.

Frequencies above the FGC servo bandwidth are minimized by a bus-to-telescope 1 Hz passive isolator, looped electrical cables, and piping that must bypass the isolator, high stiffness structures, flexures, and tuned mass dampers for particular structural resonances.

Thermal distortion causes image smear via two phenomena that do introduce non-common path effects unobservable by the star trackers and FGS. The structure between the star trackers and the FGS may induce smear of the FOV when thermal distortion causes an effective roll about the guide star that is not observable by the star tracker. This causes telescope FOV roll about the guide star in the FGS. As such, the distance from the guide star to the Instrument's FOV creates a lever arm converting roll to smear. This effect was mitigated architecturally by attaching the star tracker structure to the telescope side of the isolator, as shown in Fig. 4. This turned out to be extremely complicated to implement but the alternative of mounting a warm tracker in the cryogenic region, which would have also been very complicated. The second, much smaller effect, is caused by non-common path motion between the FGS and the rest of the instruments due to changing thermal gradients in the ISIM structure. Even smaller, second-order telescope optical effects contribute to this smear motion. These thermal distortion effects were alleviated by thermo-elastic structural design and low coefficient of thermal expansion (CTE) material choices.

## 3.2 Modeling/Model Validation

### 3.2.1 Deployed dynamics finite element model description

The jitter analysis begins with the development of a high-fidelity structural finite element model (FEM) of the deployed observatory, developed using the industry standard and reliable MSC Nastran software. The final coupled loads analysis model, designated as "FCLA2," is shown in Fig. 5. In terms of model size and fidelity, the FEM includes 3,037,406 nodes and 2,755,328 elements.

The deployed observatory-level FEM was verified in accordance with numerical quality tests specified by the project math model guidelines and empirically validated by an extensive series of tests over the course of many years. No practical, single, and end-to-end dynamics test of the deployed observatory was deemed to be possible given gravity loads, cryogenic environment affecting damping, available facilities, and integration and test cost and schedule constraints. Therefore, a series of tests were performed starting at component levels and proceeding

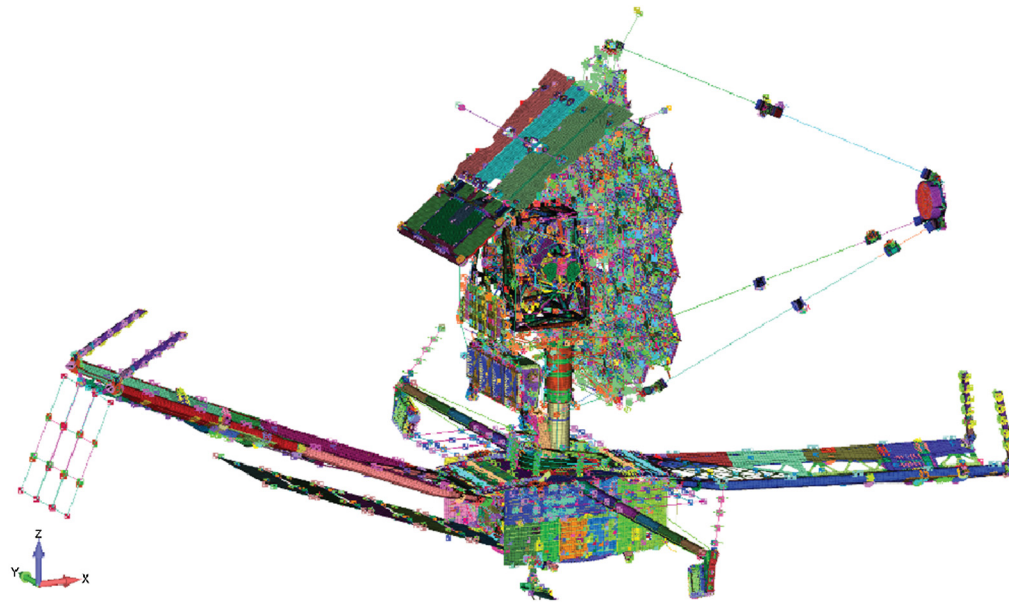


**Fig. 5** The “FCLA2” version of the finite element model (FEM) of the deployed observatory was used to verify performance requirements by analysis. This high-fidelity model was developed using the industry standard and reliable MSC Nastran software. As benchmarks of model size and fidelity, the FEM includes 3,037,406 nodes and 2,755,328 elements. A normal modes solution with the coupled mass assumption is used to predict the eigenvalues and eigenvectors (frequencies and shapes) of the resonant modes. Using a high-end cutoff of 200 Hz yields a total of 4515 modes to be retained for the jitter analysis. This fidelity results in considerable computational cost, typically requiring 3 to 4 days of CPU time for the normal modes extraction.

through assembly, subsystem, and element levels. This test campaign relied heavily on material tests and modal surveys but also included stiffness tests, sine and random vibration tests, and transmissibility tests. Transmissibility tests were key tests for all the low-stiffness assemblies in the load paths from the primary disturbances to the optics, including the vibration isolation and attenuation systems, the cryocooler heat pipes, and all wiring harnesses that could represent dynamic “shorts” across vibration isolator interfaces.

Once the FEM was assembled, Nastran’s normal modes solution, using a coupled mass assumption, was performed to predict the frequencies and corresponding shapes of the resonant modes, with a high-end cutoff of 200 Hz. This yielded a total of 4515 resonant modes retained for the jitter analysis. The equations of motion for the forced response of a multi-degree of freedom spring-mass-damper system, with a pseudo-viscous damping formulation, had been implemented in two codes, one developed at NASA’s Goddard Space Flight Center (GSFC) and one developed at Northrop Grumman Space Systems (NGSS). In both cases, the equations were modified to optionally account for the gyroscopic stiffening of the reaction wheel rotor as spin rate increases. Having two independent sets of analyses for cross-checks provided an additional layer of verification that the model results were consistent within the allowable uncertainties. On several occasions, model errors were uncovered by analysis cross-check not otherwise identified through model verification checks or validation against test data. The GSFC results were used as the basis for pre-launch verification and will be presented here.

The Nastran normal modes output was used to populate the generalized mass, damping and stiffness matrices of these end-to-end models. Damping estimates for the model came from a variety of sources. Some were strictly based on expert opinion. Some were traceable to JWST-specific tests. Finally, the damping estimates for the warm bus and sunshield structures were drawn from in-flight measurements made on prior missions. The resulting linear state-space system representation of the end-to-end model also included two linear approximations: (1) a shaping filter representing the low frequency (<0.5 Hz) roll-off due to the FGS-FSM control loop and (2) sensitivity coefficients for each optic, transforming its 6 degree of freedom (DOF) Cartesian motions into that optic’s contribution to the total pitch and yaw LOS errors.

The linear approximation of the optical model was also extended and applied as an additional set of sensitivity coefficients representing the transformation from the 6-DOF Cartesian motion of the optics to WFE. For completeness, pre-launch predictions of WFE are presented along with LOS errors in the analysis results section below. In-flight jitter measurements of WFE are still in analysis and will be the subject of future publications.

### 3.2.2 Dynamic disturbance models

Analytical models of the disturbance sources were developed. These models were validated via exported vibration tests using load cells and accelerometers to measure forces and moments in all six degrees of freedom. For the reaction wheels (RW), these measurements were made as functions of wheel spin rate, over the allowable range. Similarly, for the cryocooler compressors (CC) these measurements were made as functions of compressor drive frequency.

Reaction wheel disturbances, forces and moments, manifest as a set of discrete tones at any given wheel spin rate. One tone, the fundamental, corresponds directly to the spin rate, and other tones appear at various integer and non-integer harmonics (including one subharmonic) of the fundamental. Each individual tone has a unique amplitude, and the amplitudes of all the tones scale in unison with the square of the spin rate at low spin rates. However, measurements show that above certain spin rates, unique to individual harmonics, this square-law relation breaks down. Characteristics of the RW disturbances are also unique with respect to orientation, i.e., the axial forces, radial forces, and radial moments have different characteristics. To notionally illustrate the characteristics as described, Fig. 6 shows plots of the radial force [Fig. 6(a)] and axial force [Fig. 6(b)] disturbance profiles versus spin rate. The plots include curves for each of the harmonics in the models.

The pulse tube (PT) and Joule–Thomson (JT) compressor disturbances, forces, and moments also manifest as a set of discrete tones at any fixed drive frequency. The compressor drive frequencies are independently adjustable, with PT compressor operating in the 29.5 to 31.5 Hz range and the JT compressor operating in the 85 to 95 Hz range. Unlike the reaction wheels, all compressor disturbance harmonics appear as integer multiples of the fundamental, although similar to the reaction wheels the amplitudes of the harmonics are not identical. The disturbances manifest both as forces and moments about three orthogonal axes, i.e., six disturbance components, three forces, and three moments for each compressor. Active vibration control is employed to attenuate, but not entirely eliminate, the force disturbance component along the drive axis of each compressor.

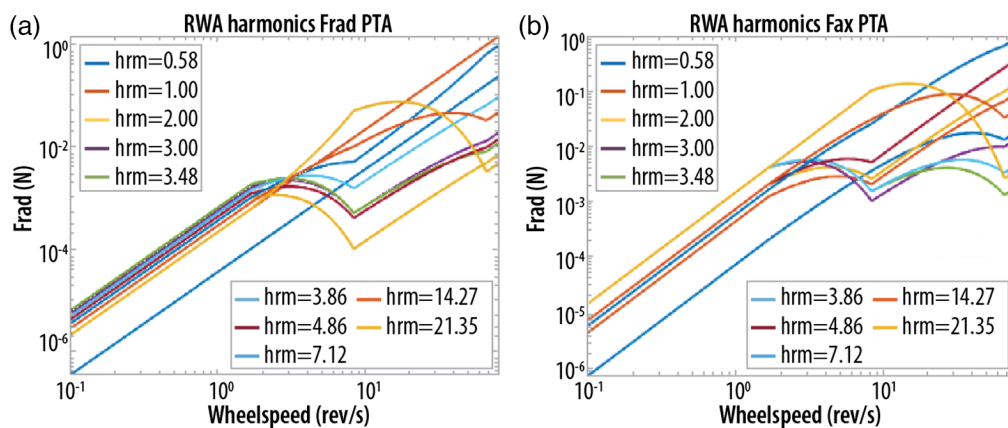


**Fig. 6** Disturbance models versus Wheel Speed for Reaction Wheel Assembly radial forces (a) and axial forces (b). The harmonics (hrm #'s) in part result from a complex set of geometric ratios unique to each make and model of reaction wheel, manifest as a series of integer and non-integer multiples of the fundamental (hrm = 1.00), which corresponds to the instantaneous wheel spin rate. Both the harmonic multiples and the relative forces (and moment) amplitudes of each harmonic cannot be predicted analytically. Rather, they are measured in a so-called “exported vibration” test, and the curves shown above, used in the end-to-end jitter analysis, are the result of curve-fits and smoothing applied to the test data.

**Table 1** MUFs applied to each of the disturbance cases defined as a function of frequency.

| Disturbance case      | MUF    |        |        |
|-----------------------|--------|--------|--------|
|                       | <20 Hz | @30 Hz | >40 Hz |
| Reaction wheels       | 1.8    | 2.3    | 2.8    |
| PT and JT compressors | 1.8    | 2.4    | 3.0    |
| Cold gas flow         | 5.5    | 6.2    | 6.9    |

The cryocooler also produces disturbances resulting from the turbulent flow of the cold gas. No tests were performed to measure this effect. The model for these disturbances was based on scaling laws found throughout standard references on classical fluid mechanics. In the absence of empirical data, validation of this model was done using high-fidelity computational fluid dynamics simulations.

### 3.2.3 Model uncertainty factors

Prior to the Mission Preliminary Design Review, a model uncertainty factor (MUF) methodology for jitter analysis was developed by a collaborative group of NGSS and GSFC experts. Fundamentally, the methodology considered model fidelity and maturity and what had been accomplished in terms of model validation while noting that at any point in time the structural components—all along the load path from disturbance to the resulting LOS predicted/measured on the focal plane—were generally at differing stages of model fidelity, model maturity, and model validity. Furthermore, the methodology accounted for inherent issues in both the underlying numerical methods and limitations in testing and model correlation, which combine to drive up model uncertainty as frequency increases. The project adjusted the MUFs for each cycle of jitter analysis throughout the development of the observatory, eventually settling on the values given in Table 1, which were used for the final integrated modeling cycle and supported the ultimate verification of multiple observatory, OTE, and spacecraft (SC)-level requirements, including Strehl ratio, EE stability, and image motion requirements.

### 3.2.4 Key analysis assumptions, methods, and pre-launch predictions

The RW-induced jitter analysis predicts LOS response subject to radial force/moment and axial force disturbances for discrete wheel harmonics through six different wheels, with the disturbances applied at the individual center-of-gravity (CG) locations in the FEM. Individual wheel responses are first determined from the cumulative responses to various forces/moments and harmonics by means of root sum square (RSS). The net LOS response as a function of wheel speed is then assessed by (a) capturing the maximum response of the six wheels for all wheel speeds below 12.5 rev/sec (750 rpm) and (b) computing the RSS response of the four worst wheels for wheel speeds above 12.5 rev/sec.

The effect of the ACS “push-through” algorithm (PTA) is also included in the analysis. The PTA uses the principle that a steady-state response will not develop if the wheels are swept fast through resonance. Accordingly, the damping for low-frequency modes affected by the use of the PTA is artificially, but precisely, increased to approximate this effect. This damping adjustment is not made for the CC-induced jitter analysis. Due to the observed jitter performance on-orbit, the PTA was not activated in the ACS, which enables improved momentum management performance.

Finally, since cryogenic damping is very low and responses typically have very narrow frequency bands, a reaction wheel would spend very little time at peak resonance. Therefore, for reporting of results for the reaction wheel disturbance, a criterion was developed whereby the 99.7<sup>th</sup> percentile response is reported instead of the actual peak response.

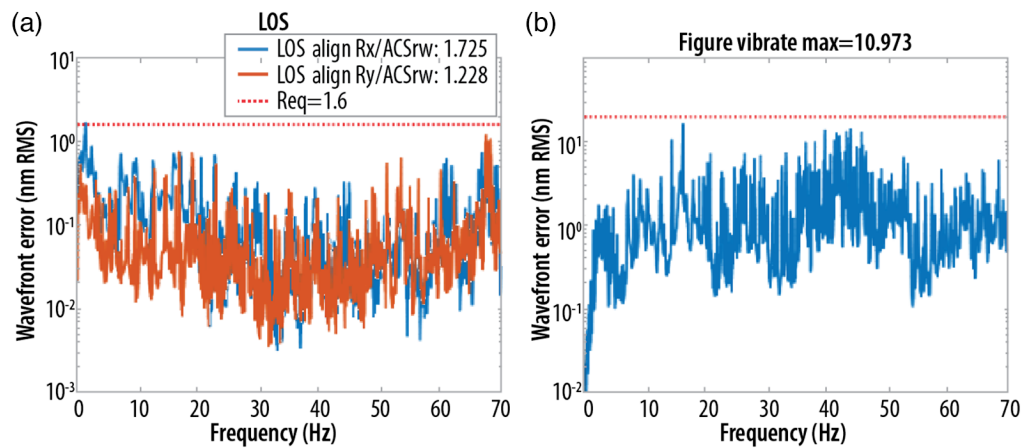


**Fig. 7** LOS and WFE performance versus reaction wheel speed. On the left is shown the predicted LOS (in milli-arcseconds, or “mas”) responses about the V2 (“Rx”) and V3 (“Ry”) axes as functions of RW spin rate (in Hz), with the 99.7<sup>th</sup> percentiles noted in the legend. The dashed horizontal line indicates the allocation (not requirement) for this contribution to LOS error, per the image motion error budget. On the right is shown the predicted WFE (WFE, in nm RMS) response resulting from PM segment motions, also plotted as a function of RW spin rate and against the corresponding budget allocation. The analysis results indicated that the LOS error would slightly exceed (1.7 mas predicted versus 1.6 mas allocated) the threshold and only at one peak at  $\sim 2$  Hz (wheel speed of 2 rev/sec). These results were accepted, as other analyses had shown adequate margins in the other branches of the image motion error budget.

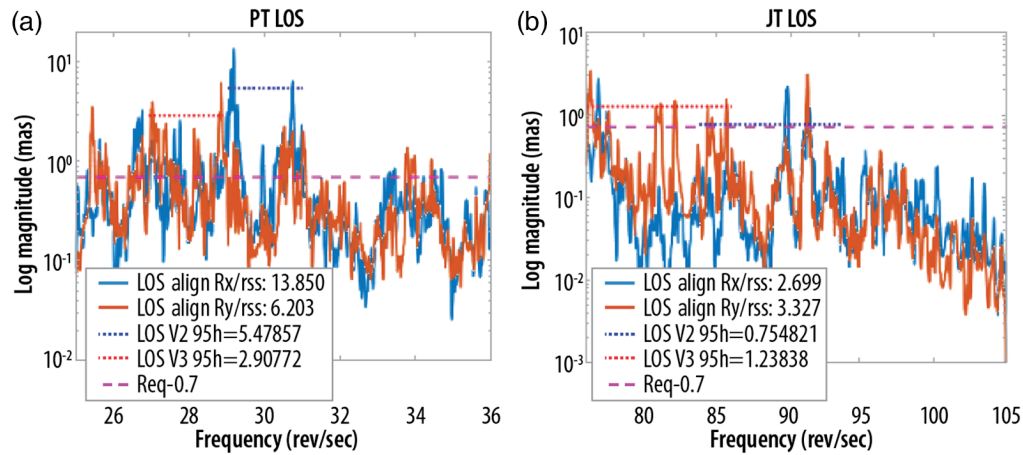
Figure 7 presents two plots. Figure 7(a) shows the predicted LOS (in milli-arcseconds) responses about the V2 (“Rx”) and V3 (“Ry”) axes as functions of RW spin rate (in Hz), with the 99.7<sup>th</sup> percentile responses noted in the legend. The dashed horizontal line indicates the allocation (not requirement) for this contribution to LOS error, per the image motion error budget. Figure 7(b) shows the predicted wavefront (surface figure error, in nm RMS) response resulting from PM segment motions, also plotted as a function of RW spin rate and against the corresponding budget allocation.

The cryocooler PT compressor-induced jitter is analyzed through applying force/moment disturbances and the associated harmonics at the compressor CG frequency range of evaluation spans within 10% of the variable compressor speed band (with respect to the nominal drive frequency) to account for frequency uncertainty in the Nastran normal modes solution. The total response is obtained through the RSS of responses contributed by the various forces, moments, and harmonics. The 95<sup>th</sup> percentile response that excludes the worst 5% of the compressor speed within a sliding 2 Hz wide evaluation frequency range is reported. A similar analytical approach is used to evaluate JT compressor-induced jitter. In addition to the reported PT and JT jitter predictions, since the cooler operating frequencies are tunable, a separate analysis is made to calculate the predicted number of possible operating frequencies, which falls above a Strehl ratio of 0.99.

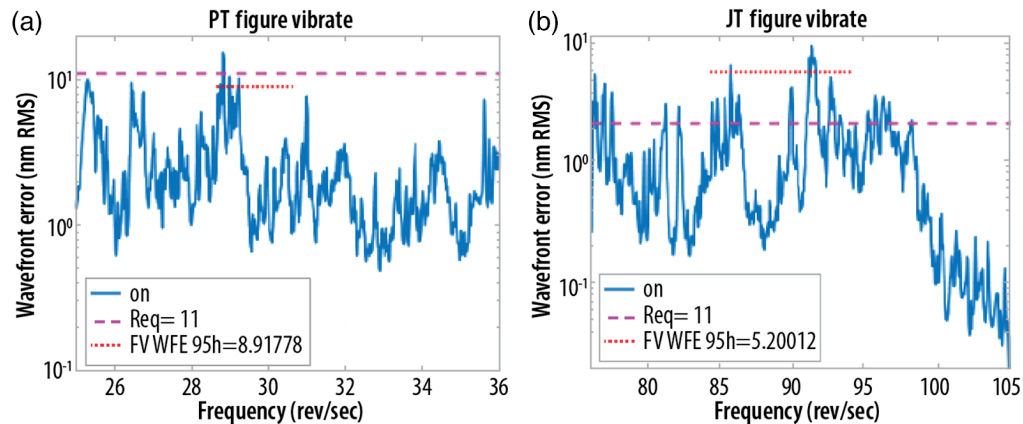
Figure 8 presents the LOS responses due to PT [Fig. 8(a)] and JT [Fig. 8(b)] compressor disturbances, about both the V2 (“Rx”) and V3 (“Ry”) axes. As noted, to account for resonant mode uncertainties the analysis frequency range extends beyond the compressor drive speed ranges. In the legends, both the peak and 95<sup>th</sup> percentile responses (in mas) are reported on a per-axis basis.

Figure 9 presents the corresponding WFE responses due to PT [Fig. 9(a)] and JT [Fig. 9(b)] compressor disturbances.

As shown in Figs. 8 and 9, there could be exceedances to the WFE and LOS requirements depending on the drive frequencies of the PT and JT compressors. Since these drive frequencies are adjustable once on-orbit, a cryo-cooler tuning procedure was developed to sweep the PT and JT compressor drive frequencies until the WFE and LOS are reduced to acceptable levels. As it turns out, it was not necessary to execute this tuning procedure on orbit.



**Fig. 8** LOS performance versus PT and JT compressor speed. Here the LOS responses are due to the PT (a) and the JT (b) compressor disturbances, about both the V2 (“Rx”) and V3 (“Ry”) axes. To account for structural resonant mode uncertainties, the analysis frequency range extends beyond the compressor drive speed ranges. In the legends, both the peak and 95<sup>th</sup> percentile responses (in mas) are reported on a per-axis basis. In the case of the PT compressor, many response peaks exceeded the allocation of 0.7 mas, some significantly (worst case of 13.9 mas). However, the compressor drive speeds can be systematically adjusted, whereas at the same time the LOS error can be measured. An analysis of this “cooler tuning” operation indicated an acceptable probability of successfully identifying gaps between the peaks and adjusting the compressors to operate at the new set points. For this reason, as well as the adequate margins in the other branches of the image motion error budget, these results were also accepted.



**Fig. 9** WFE performance versus PT and JT compressor speed. These plots present the WFE (WFE, in nm rms) responses due to PT (a) and JT (b) compressor disturbances. Far fewer response peaks exceed the allocations, compared to the LOS results, increasing the likelihood that on-orbit tuning, if necessary, would be successful. Once again, these results were considered acceptable even with the exceedances.

Cold gas flow manifests as both a pulsating disturbance (at the JT compressor drive frequency) and a random disturbance, which is assumed to be white noise (flat spectrum) from 0 to 200 Hz with amplitude tuned to match a prescribed RMS value. Pulsating jitter analysis is performed by applying the force disturbances directly at the MIRI CG. The cumulative response is obtained through the RSS of responses contributed by the forces in different axes, and the frequency evaluation range is consistent with the JT compressor jitter analysis. The 95<sup>th</sup> percentile number for pulsating jitter is reported. Random vibration jitter is analyzed by applying the force disturbances at various locations distributed within the ISIM bench and along the path of the cooler tower assembly and refrigerant line deployment assembly. The output power spectral density (PSD) includes the RSS responses from the forces at different points of application.

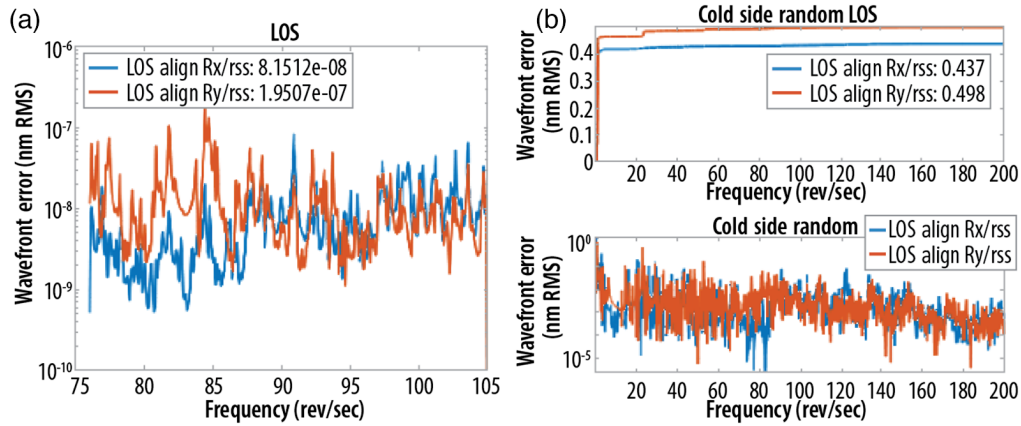


**Fig. 10** LOS performance due to cold gas flow. These plots present the LOS responses in mas, about both the V2 (“Rx”) and V3 (“Ry”) axes, due to the pulsating (a) and random (b) components of the cold gas flow disturbance. The response due to the pulsating effect is effectively negligible and is taken as 0.0 mas for practical purposes. Two plots are shown on the right for the random disturbance analysis. The top plot shows the cumulative RMS (integral of the PSD), and the bottom plot shows the PSD response itself. The response due to the random flow noise is much higher than that due to the pulsating component but is still less than the allocated value.

The resulting LOS response is then computed by integrating the output PSD response over the evaluation frequency range.

Figure 10 presents the LOS response due to both the pulsating [Fig. 10(a)] and random [Fig. 10(b)] components of the cold gas flow disturbance. The response due to the pulsating effect is effectively negligible and is reported as such (0.0 mas) below in the results summary table. Two plots are shown on the right for the random disturbance analysis. The top plot shows the cumulative RMS (integral of the PSD), and the bottom plot shows the PSD response.

Figure 11 presents the corresponding WFE response due to both the pulsating [Fig. 11(a)] and random [Fig. 11(b)] components of the cold gas flow disturbance. Once again the response due to the pulsating effect is effectively negligible and is reported as such (0.0 nm) below in the results summary table. Two plots are shown on the right for the random disturbance analysis.

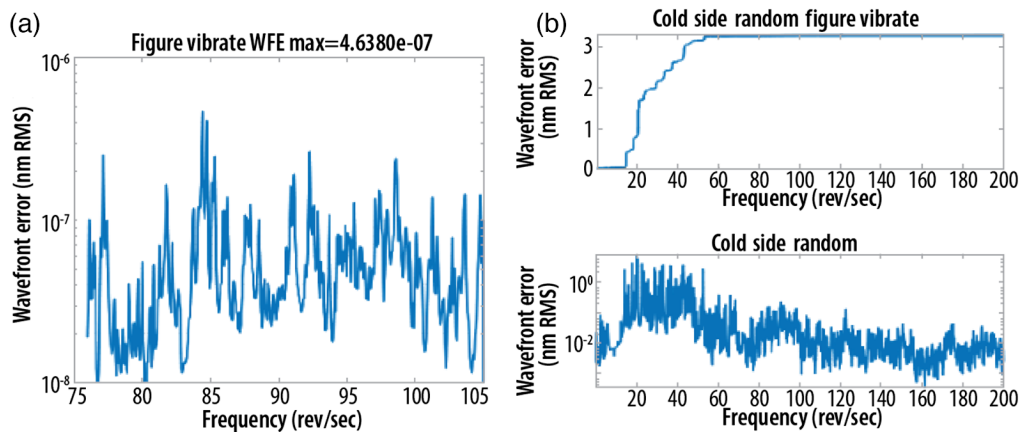


**Fig. 11** WFE performance due to cold gas flow. Similar to the previous figure, these plots present the WFE (WFE, in nm rms) responses due to the pulsating (a) and random (b) components of the cold gas flow disturbance. As is the case for LOS, the WFE response due to the pulsating effect is effectively negligible and is considered to be 0.0 nm for practical purposes. Two plots are shown on the right for the random disturbance analysis. The bottom plot shows the PSD response, and the bottom plot shows the cumulative RMS. And again as is the case for LOS, the WFE response due to the random flow noise is much higher than that due to the pulsating component, but still less than the allocated value.

**Table 2** Integrated modeling jitter analysis results shown with respect to the LOS allocations and the WFE equivalents.

| Disturbance          | LOS (mas)  |           |           | WFE (nm)   |           |
|----------------------|------------|-----------|-----------|------------|-----------|
|                      | Allocation | V2        | V3        | Allocation | PM figure |
| Reaction wheels      | 1.6        | 1.7       | 0.5       | 13         | 11.0      |
| PT compressor        | 0.7        | 5.5 (2.2) | 2.9 (2.1) | 11         | 8.9 (4.9) |
| JT compressor        | 0.7        | 0.8 (0.8) | 1.2 (0.5) | 2          | 5.2 (4.9) |
| Cold gas – pulsating | 0.1        | 0.00      | 0.0       | 1          | 0.0       |
| Cold gas – random    | 0.7        | 0.4       | 0.5       | 5          | 3.3       |

The top plot shows the cumulative RMS (integral of the PSD), and the bottom plot shows the PSD response.

The results from these analysis cases are summarized in Table 2. For the PT and JT compressor results, the values in parentheses reflect the results of on-orbit tuning (drive frequency adjustments) had it turned out that tuning was necessary—which was not the case. These results were based on conservative assumptions, including the MUFs, and simulated worst-case operational scenarios since the analyses were performed to verify that JWST met its requirements. Exceedances relative to the allocations were allowed as long as the corresponding parent requirements were satisfied, as a result of margin reported by other analyses.

### 3.3 Fine Guidance Control Loop

As shown in Fig. 3, the main contributor to the LOS performance was the jitter within the fine guidance control bandwidth. Developing high fidelity simulators was key to validating the models, in particular of the ACS and the FGS ingesting realistic images, with PSFs covering normal operations as well as the different phases of commissioning while the mirrors were being aligned. This allowed the operations between ACS and FGS on its control loop to be tuned and demonstrated; the validation of the on-board software commanding handshake between them; the identification of updated software parameters that would allow the loop to be closed using segmented mirrors and throughout the alignment process; and end-to-end testing of many different flight operations. Those simulators had to also meet the millisecond flight timing on the various components to provide adequate responses.

End-to-end hardware testing involving all the components and their flight-like interactions was not possible but many portions that could be tested stand alone were identified.<sup>4</sup> Executing those tests with the flight hardware to reduce risk was key as well. Another important portion was identifying timing budgets for the different operations and checking those timing operations out incrementally. A critical timing check was the guider to FSM loop, which was tested during the cryogenic test by injecting a periodic change into the FSM.

Another critical aspect of pointing stability was the inter-boresight drift between the guider and instruments, which is covered later in Sec. 4.5.1.

### 3.4 On-Orbit Results

*In situ* measurements of jitter were obtained during the commissioning phase once wavefront and NIRCcam commissioning had progressed to the point where calibration star PSFs were of sufficient quality to be tracked and captured using  $8 \times 8$  pixel windows, at a 2.2 milli-second frame rate. The PSF centroid time histories, roughly 2 min duration ( $\sim 50,000$  samples) were converted to jitter power spectral densities and plotted from 0 to 227 Hz (the Nyquist rate) revealing spectra characterized by a broadband noise floor (due to sampling artifacts) and any number of discrete tones standing out above the noise. The cryocooler state data and reaction wheel tachometer data corresponding to the jitter samples was also downloaded. Figure 12 illustrates the image data collection and analysis process.

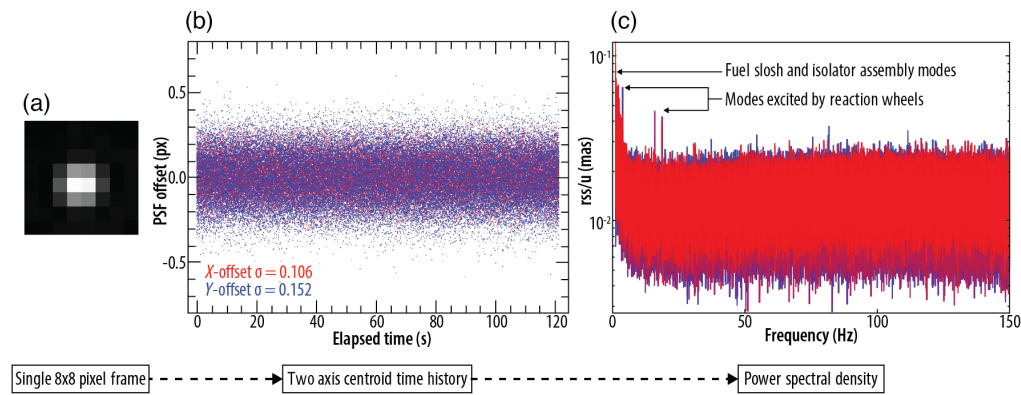


**Fig. 12** Representative on-orbit centroid measurement and analysis results, showing the single  $8 \times 8$  pixel frame (a), the two-axis centroid time history (b), and the power spectral density of the measurements (c). These plots notionally illustrate the process developed to measure image centroid data at high speed (2.2 msec frame rate) by capturing a series of  $8 \times 8$  pixel subarrays using the NIRCam instrument. The frames are captured for a period of approximately 2 min ( $\sim 50,000$  samples), and the two-axis centroid time histories are computed. The time histories are converted to a power spectral density for analysis, which includes removing measurement artifacts. The representative spectrum presented in the right-hand plot shows no tones or harmonics due to either the PT or JT compressors. Several of the more significant peaks in the spectrum appear at frequencies corresponding to reaction wheel speeds, measured via tachometers, during the 2-min window. The most dominant responses correlate with the fuel slosh modes and bending modes of the Isolator Assembly. The measurements had been taken immediately following a slew maneuver, and these modes did not have time to sufficiently dampen when the centroid data were obtained.

Having collected and analyzed the jitter data for several months, a number of general observations were made.

1. The pre-launch analysis had over-predicted jitter. As noted, the analysis supported requirements verification, and hence relied on multiple conservative assumptions. None of the pre-launch analysis stripped away the conservatism to estimate the nominal (much less the best case) performance.
2. No tones were observed at frequencies corresponding to the drive frequencies of either the PT or JT compressors, nor the harmonics of those drive frequencies [see Fig. 12(c)]. This result eliminated the need for cryocooler tuning.
3. Dominant tones have been observed at very low frequencies of about 0.04 and 0.3 Hz, below those corresponding to the reaction wheel speeds at the times the measurements were made.<sup>5</sup> Jitter predictions with the wheels running at the observed speeds would not have predicted any response at all at those lower frequencies, which correspond to the predicted 0.04 Hz fuel slosh modes and to the 0.3 Hz rocking modes of the Isolator Assembly that separates the SC and sunshield from the telescope and science instruments. The conclusion, therefore, is that these modes are being excited by slews or momentum unloads, which had been executed shortly before the jitter measurements were made, and that the response of those modes had not completely abated due to damping.
4. No significant tones were observed at frequencies corresponding to other low-frequency ( $<12.5$  Hz) resonant modes. This result eliminated the need to employ the reaction wheel PTA.
5. Only a relatively small number of tones were identified at frequencies corresponding to reaction wheel speeds, or known harmonics of those speeds, at the time the jitter measurements were obtained. Therefore, the observation that reaction wheel signatures were not always present in the spectra is unsurprising. Wheel speeds varied from measurement-to-measurement and it was only predicted to see discernible signature tones when wheels happened to align with significant resonant modes, which are at fixed frequencies. Still, more evidence had been expected, and the majority of the post-launch analysis effort was an attempt to understand this result.

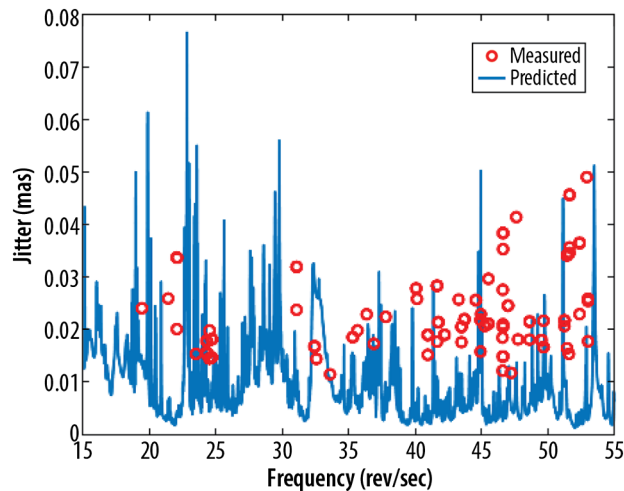


**Fig. 13** Revised reaction wheel predictions (red circles) compared to jitter measurements (blue line). Having removed all conservative assumptions and analytical methods used for the case of pre-launch (verification) predictions, the predicted LOS response due to reaction wheel six magnitudes compare well on average with measured response.

One question that needed to be addressed was the possibility that the wheel speeds were changing quickly enough during the measurements for the resonant responses to be artificially damped—exactly the same effect the PTA was designed to achieve as a jitter mitigation for problematic modes. The analysis only evaluated the steady-state jitter as a function of wheel speed. However, the tachometer data showed that, while the speeds did change during the elapsed time for the jitter measurements, the effect would have been negligible at best.

Next, a number of adjustments were made to remove as much conservatism as practical from the analysis, before repeating it. The MUFs were removed, as well as “knockdowns” applied to damping estimates. Damping adjustments for low-frequency models that had been made assuming the PTA was operational were removed. An alternative and less-conservative reaction wheel disturbance model was used. Finally, the reaction wheel isolator properties were adjusted to better reflect actual flight temperatures. To be conservative, the pre-launch analysis used the thermal cold-case (5°C) properties for the viscoelastic material, increasing isolator stiffness and reducing isolator damping. For the new analysis, the viscoelastic material properties were adjusted to the thermal nominal case (20°C), resulting in softer, more well-damped isolators.

The end-to-end reaction wheel jitter analysis was then repeated for each of the six wheels, but only at the wheel speeds contained in the data set. As an example, Fig. 13 shows the results for the comparison using data for reaction wheel No. 6 (RW6).

A total of 76 tones were correlated with RW6 at known harmonics (note: in some cases, the response is due to RW6 plus another wheel). With all the conservatisms removed from the analysis, we were able to obtain rather favorable comparisons between revised predictions and measurements, at least in terms of response magnitude. However, the predictions generally exceed the measurements at lower frequencies (<35 Hz) and generally fall below the measurements at higher frequencies (>35 Hz). This is reasonably consistent with expectations given the assumed  $\pm 10\%$  uncertainty in predicted frequency of the structural resonant modes and the non-continuous sampling of wheel speeds resulting from the “measurements of opportunity” approach.

### 3.5 Dynamic Stability Lessons Learned

There were several lessons learned in architecting, modeling, and testing the dynamic stability of JWST.

1. The approach of applying MUFs as the equivalent to hardware fabrication tolerances in the error budget allocation was a novel concept at the JWST mission start and proved to be a successful process. MUFs also provided a systematic model validation success criteria when comparing analytical prediction to test data and for detecting workmanship issues. For future applications, more rigorous means of quantifying uncertainty through multi-

disciplinary probabilistic analyses managed at the system level would avoid assigning MUF values through ad-hoc methods at the individual discipline level, which could lead to higher estimates and double bookkeeping of uncertainties.

2. The MUF values published in this paper are specific to JWST's design, materials, environment, and performance goals. They should not be used on other projects without performing their own uncertainty analyses.
3. While the worst-case analysis conditions did not exceed the error budget allocations for JWST and provided hidden margin for unknowns, it did over-predict what is being experienced during normal operating conditions on-orbit. For future missions, the worst-case operations assumption may prove too conservative for extreme stability requirements and may in fact drive the design beyond what is necessary. It is recommended that simulations representing the "day-in-the-life" augment the worst case analysis conditions to better assess sensitivity to such assumptions and allow for graceful degradations or operations mitigations.
4. The use of model cross-checks performed by independent teams of analysts has proven to be an effective method for detecting subtle model errors early when not otherwise identified through standard model verification methods, for challenging model assumptions of complex physics, and ahead of model validation tests. When results are shown to be the same within the allowed model uncertainties, model cross-checks provide credibility of the complex analysis predictions for risk reduction.
5. Flight models and model delivery must be treated with the same rigor as flight hardware as to provide credibility of the predictions used to verify requirements. This is especially important when elements of the models are being delivered by different teams and contractors, along with delivery of the corresponding flight hardware. This includes early project requirements on model configuration, configuration management, interfaces, analysis processes, model uncertainty posture, verification and validation, and expected reviews and documentation. These models also include those supporting tests in the test configuration.

## 4 Thermo-Mechanical Stability

### 4.1 Architecture

The entirety of the JWST telescope assembly, which includes the PM, SM, and Aft Optics System (AOS) optical elements and their supporting metering structures, is not actively thermal controlled. The telescope components shown in Fig. 14 reside on the cold side of the sunshield and are subject to small temperature fluctuations as the observatory is pointed to view different targets that change the thermal boundary conditions. The thermal management elements were

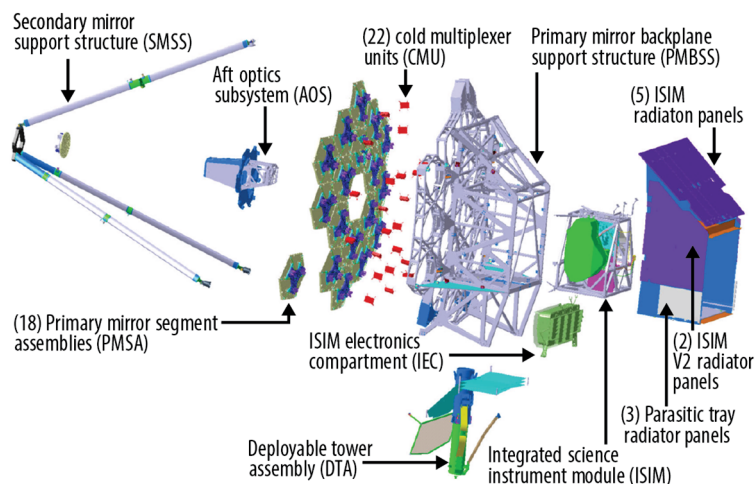


**Fig. 14** The JWST OTE is on the cold side of the observatory and passively stabilized to mitigate the optical effects of temperature variations experienced while the observatory points within its field of regard.

designed principally to achieve and maintain the crucial operating temperatures necessary for the science. The resulting thermal environment fluctuations were subsequently managed by engineering material designs and combinations to essentially athermalize the telescope assembly to achieve the requisite operational dimensional stability across all pointings within the field of regard.

A system that is athermalized is sufficiently immune to temperature variations to still maintain the optical stability during data collection operations. The JWST telescope design chose materials with near-zero CTE over the operational temperature range or engineering a combination of materials with non-zero CTE to achieve a near-zero net effect.

The optical mirror elements (PMSA, SM, and AOS optics) and the AOS support frame are fabricated from Beryllium, which inherently has a stable near-zero CTE at temperatures below 50 K where the telescope operates. However, the actuator systems that position and align the various optical elements use other materials, so clever combinations of materials and how they are packaged were engineered to achieve the necessary performance.

The metering structures that include the PMBA, the SM support structure (SMSS), and the backplane support frame (BSF) are sophisticated assemblies that consist of structural elements, connecting interfaces, and deployment mechanisms. The mix of materials required achieving an athermalized design by customizing the CTE of the composite structural elements to offset the influence of the several non-zero CTE components in the mechanisms, invar fittings, adhesives, and mounted electronics equipment. The tailoring of the composite materials varied spatially across the telescope in response to the overall packaging of the system. The metering structure had the additional task of supporting all the optical elements, the ISIM, and other critical items like the instrument thermal radiators during launch. Consequently, the structure had to meet high performance dimensional stability performance at cryo temperatures and endure the harshness of the launch environment.

The final backplane design is shown (partially) with mirrors being installed in Fig. 15. This backplane structure had over 100 laminate variants and several hundred custom piece-parts that all had to be fabricated, inspected, and assembled to an impressive geometric tolerance requirement. The large number of piece-parts help with stability performance because no single piece has a far reaching influence on the shape variations. Also, each composite tube was built with random mixing of prepreg lots to manage lot-to-lot variations in the composite properties.

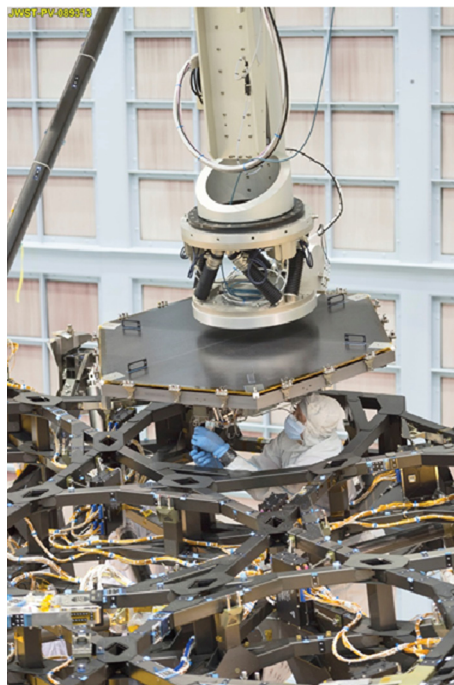


**Fig. 15** Robotic installation of a PM segment to the backplane assembly at GSFC.

The performance of the telescope depends also on the correctness of the assembled geometry. Variations in the as-built geometry can print through as a variant in the anticipated spatial content distribution associated with thermal changes. This effect is a consequence of the direct influence geometry has on stiffness. There is a similar influence from integration loads that store strain energy at critical interfaces. Stored energy can release unexpectedly and introduce spurious behaviors to the system. The JWST telescope assembly, from individual piece parts to completed subassemblies and assemblies, were prescribed strict controlling assembly, integration, and testing tolerances to achieve the necessary precision of the geometric aspects.

## 4.2 Modeling and Technology

The JWST Technical Non-Advocate Review board reviewed and assessed several critical technologies requiring maturation during the first years of the program. The composite structure PM backplane was one of these critical technologies. There were two elements that required demonstration. First was the general question if a composite structure can be engineered to meet the PM figure stability requirements. This was the first time a large segmented PM was installed atop a composite backplane. The architecture essentially imposes not only PM positional alignment stability requirements but also includes PM spatial figure budget allocation. This had never been required of a composite structure. Second, the program verification plan for backplane figure stability performance was done by analysis. The backplane figure stability was not measured by test prior to integration of the OTE assembly. This demanded developing and validating an analysis process that could reliably predict the dimensional influence of the BP on PM figure due to temperature changes at cryogenic temperatures.

The backplane stability test article (BSTA) and the subsequent test campaign were the response to the two elements of this critical technology demonstration. The details and results of the BSTA test have been reported previously.<sup>6</sup>

Flight backplane stability testing for the AOS-ISIM interface stability was within the model prediction uncertainty and met requirements. Ground support equipment (GSE) and metrology system performance had to be equally or more stable than the article in test and required an engineered metrology support bench and optical metrology system.

## 4.3 Composite Coupons and Subsystem

The path to the flight backplane metering structure covered approximately 15 years before delivery of the final article. The long duration was a combination of factors ranging from the need to do iterative design for lightweighting, the need to carefully design cryogenic adhesive joints; the large number of interfaces; the large number of components, which impacted manufacturing; and the complex assembly and test programs. The backplane was designed for mass optimization and had challenging performance requirements especially at cryogenic temperatures. The early work included technology investments, both private and government, and followed with program funded activities.

### 4.3.1 Building block approach

The backplane development path followed a building block approach starting with the simplest elements and getting more complex. The principal test and demonstration events and some of their objectives are listed below.

1. Deployable optical telescope article (DOTA): a large hinged/latched composite structure. This demonstrated large composite assembly performance at cryogenic temperatures, engineering models for design and analysis, hingeline latch stability at cryogenic temperatures, and the ability to test large scale articles at cryogenic to nanometer level measurements.
2. BSTA: a 1/6th portion of the backplane. This anchored method for engineering of stable composite structures with nm level performance, validated analysis methods and models to support flight hardware acceptance by analysis for dimensional stability performance and demonstrated the ability to measure composite structure stability at cryogenic conditions.
3. Engineering development analysis verification test articles. This validated analysis model at feature level, such as bonded structure nodes.
4. Additional stability testing at the telescope level (covered in a later section).

### 4.3.2 Composite Subsystem Lessons Learned

The thermomechanical stability tests were all successfully completed, with several important lessons learned. The lessons cover a wide range of aspects including the modeling techniques, model requirements, fabrication, and test approaches.

The first category of lessons learned was in the modeling methods. The finite element analysis (FEA) modeling techniques are adequate tools for this type of analysis. Mesh refinement required a rigorous convergence process and resulted in a high resolution thermal-mechanical model of the backplane (the flight backplane model had  $\sim 4.4$  M degrees of freedom). A stochastic analysis method was necessary to properly quantify model uncertainty and apply the required MUFs. The stochastic analysis for the BSTA used to validate the technology included developing influence functions for over 10,000 variables in the model. BSTA ultimately confirmed a composite backplane can be made stable to nanometer levels at cryogenic temperatures. This test validation of the FEA model enabled accurate system-level budgeting was used to improve the manufacturing approach and develop a high confidence test plan.

The second general category of lessons learned was FEA model requirements. From the DOTA, we learned solid elements that capture three-dimensional elasticity effects are necessary. Shell and beam elements are at risk of producing misleading results unless it has been shown that the components being represented have minimal influence on the final results. One should plan to include all components including all pieceparts, fittings, adhesive volumes, and any attaching components. No part is left off by assumption of being inconsequential but must be shown definitively in the stochastic analysis to have influence below the threshold limit. In addition, validated material models are required. This starts with a stochastic analysis that identifies the critical material properties needed with a prescribed uncertainty limit. For example, the coefficient of thermal expansion was identified as a primary material property for all materials. However, sensitivity studies of CTE variations identified that CTE measurement accuracy of better than 10 ppb as a function of temperature down to 30 K was necessary to achieve performance. No facility existed that could produce both the CTE data accuracy and testing throughput to support flight production so multiple facilities had to be made. A high-accuracy cryogenic dilatometer was designed at the Jet Propulsion Laboratory (JPL), which achieved the measurement accuracy goals and provided early evaluation of relevant material samples.<sup>7</sup> The JPL CTE method was later enhanced and replaced at the Southwest Research Institute to allow testing of composite tubes and higher throughput for flight production.<sup>8</sup> An additional detail was that knowledge uncertainty of common materials, including metals and adhesives, demanded the same advanced testing requirements and knowledge as the composite.

The structural fabrication process needed to be carefully controlled. Another key lesson was that sensitivity to bond joint adhesive volume, particularly thickness, was almost as significant as to CTE. All bond line thicknesses were measured and verified during integration. Ultimately more than 8000 bonds were accomplished with less than 10 discrepancies that were either reworked to meet specifications or shown by analysis to be acceptable in the particular location.

The final category of lessons learned were verification metrology, GSE, and facilities. Element-level tests did not provide the anticipated value because the required engineering and ultimate complexity of the test did not produce useful results early in the program. Designing a test to validate a model to these levels is as big a challenge as designing the flight element itself. The BSTA metrology system required development of a new type of speckle interferometer to properly perform the test.<sup>9</sup> GSE influence on the performance of the test article needed to be minimal, ideally zero. The BSTA test was performed in the X-Ray Calibration Facility at the Marshall Space Flight Center (MSFC). Interfacing with preexisting test facilities involves extensive pre-planning activities and rigorous and formal test plan execution.

## 4.4 System Testing and Associated Issues

The test program for JWST was comprehensive and included inspection, model validation, verification tests and crosschecks. System-level stability could not be directly tested and therefore model validation efforts were the primary method of verification. However, the modeling validations assume the flight configuration is as-designed. Direct inspections or tests are still needed

to confirm that workmanship met the design intent. The team did plan workmanship checks for stability, though not initially with the same level of formal approach as was used for wavefront measurements. In addition, the large amount of soft structure and the risks of deployment snags made inspections and audits critical, with many modifications added late in the development phase to improve the process. The below sections describe the tests and lessons learned.

#### 4.4.1 Test overview and objectives

The optical telescope element and integrated science instrument module (OTIS) integration and test program culminated with a cryo-vacuum test of the telescope and science instruments conducted in Johnson Space Center (JSC) Chamber A from July to October 2017. Prior to the cryo-vacuum test, the OTIS was subjected to ambient launch environments testing including sine vibration, acoustics, and associated pre/post environmental ambient functionals. The broad objectives of the cryo-vacuum test were to verify functional, thermal, and optical performance requirements in the cryogenic flight operating temperature environment and provide data for model validation. All of the objectives of the test were met, including verifying performance following ambient environments,<sup>10</sup> optical verifications,<sup>11</sup> thermal balance testing and associated thermal model correlation,<sup>12</sup> and thermal distortion stability testing and associated model validation. The thermal distortion stability tests were performed to validate analytical models used to predict thermo-mechanical stability and included tests dedicated to measuring alignment stability between the PM and SM and PM figure stability associated with an imposed change in operating temperature environment. The thermal distortion stability test focused on validation of the structural model as subjected to the measured temperatures during OTIS testing, which thermally was neither the temperature profile nor the steady-state expected on-orbit. Because there were many more structural nodes in the FEM than the limited number of test thermal sensors, numerical techniques were needed to map the expected temperatures to all FEM nodes. This technique could not be applied on-orbit because there are even fewer flight thermal sensors and their accuracy is not sufficient to capture the milli-Kelvin changes expected following a slew. The following sections will discuss the test setup, optical test equipment, and test results relating to thermo-mechanical stability.

#### 4.4.2 Test setup and optical test equipment

The test setup for the OTIS cryovacuum test in JSC Chamber A is shown in Fig. 16. The flight OTIS was suspended from a vibration isolation system at the top of the chamber during the test.

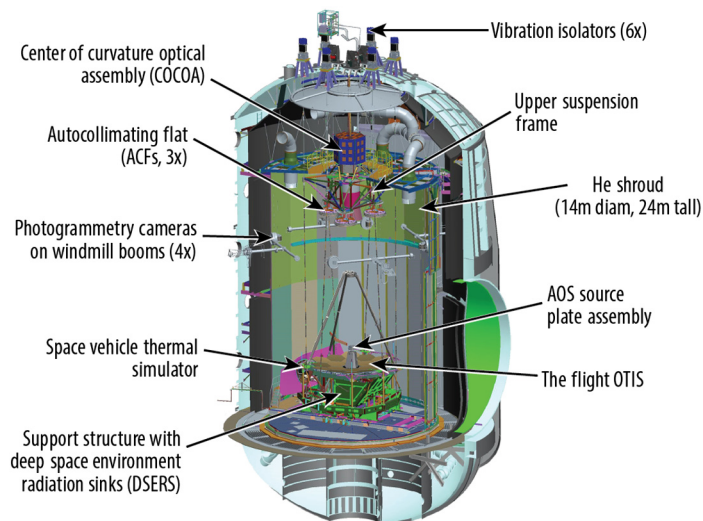


**Fig. 16** OTIS cryo-vacuum test configuration showing the telescope inside the chamber with optical metrology test equipment.

The thermal environment was maintained by an inner helium shroud/outer nitrogen shroud to control the global thermal environment and a system of deep space edge radiation sinks to locally maintain the temperature at the OTE/ISIM radiators and a space vehicle thermal simulator at the boundary between the OTIS and the rest of the JWST observatory that was not present for the test. The optical test equipment used for the cryogenic testing was designed specifically for the measurements needed.<sup>13</sup> The key components included the Center of Curvature Optical Assembly (CoCOA<sup>14</sup>), which included interferometers to measure the surface figure of the entire PM; a photogrammetry (PG) system of cameras on four rotating booms<sup>15</sup> to measure the relative positions of optical targets over on the flight hardware and test equipment; the AOS Source Plate Assembly, which provided light sources at the intermediate Cassegrain focus of the OTE for use in downward (half-pass) imaging and upward (pass-and-a-half) imaging (in conjunction with three autocollimating flats); and fiducial light strips around the edges of the PM for measuring pupil shear and vignetting.

#### 4.4.3 Thermal distortion stability testing

The overall approach to thermal distortion stability testing was to characterize the system optically at stable operating temperature, apply a temperature perturbation, and then track the change in optical performance from the baseline state due to the thermal perturbation. On-orbit thermal stability is on the order of 10's of milli-Kelvin during in typical operations (150 mK in design space) and results in corresponding thermo-mechanically induced optical performance changes on the order of a few tens of nanometers in surface figure worst-case and hundreds of microns in SM alignment shift.

Because of the small expected changes due to temperature, it was not feasible to induce flight like temperature perturbations and measure flight-like thermo-mechanical response during ground tests, so the program took the approach of performing “over-drive” tests where a large (relative to flight) thermal perturbation was applied resulting in optical changes within the measurement capabilities of the optical test equipment and then using the test data to validate analytical models that were then used to predict and verify on orbit performance. Two types of thermal distortion tests were performed: PM figure drift and alignment drift.

The PM figure drift test used the CoCOA interferometers to measure the change in PM surface figure (RMS WFE) due to a change in temperature during a portion of the cooldown phase of the test as the telescope approached operating temperatures. The alignment drift test used the PG system to measure the change in alignment between the PM and SM due to a change in temperature during both the cooldown and warm-up phases of the test. In the case of both tests, temperature measurements from thermal sensors were used as part of distortion analyses performed with finite element structural models to predict performance in-test. Model validation was completed by comparing measurements from the test with predictions from analytical models including a MUF established by the program. The success criterion was that model predictions, including MUF envelope test measurements, which includes measurement uncertainty. Predictions from the thermal distortion model incorporating measured temperatures from the test demonstrated the same trend in delta WFE as observed in the test with the measurements bounded by the 1.6 MUF at all times. The final RMS WFE measurement over the overdrive 3 K average change in temperature of the backplane was 1579 nm RMS (cf., <40 mK following a worse case slew in flight), with an observed uncertainty of  $\pm 25$  nm. The model prediction was 1403 nm RMS. The uncertainty on the model predictions were determined from pretest analyses to be  $\pm 275$  nm for this analysis. The alignment drift test and associated model validation proved to be more challenging. The overall objective of validating the MUF was the same for this test; however the predicted magnitude of the alignment drift due to the temperature changes experienced in-test was less than the PG uncertainty measuring it, making it difficult to meet the validation objectives. The alignment drift test results did demonstrate that the MUF used in on-orbit predictions was consistent with expected uncertainties and there were no major modeling errors. As presented in Sec. 4.5, on-orbit performance met or exceeded expectations based on pre-flight predictions, further supporting the validity of the thermo-mechanical modeling and conservatism of the MUF predictions.

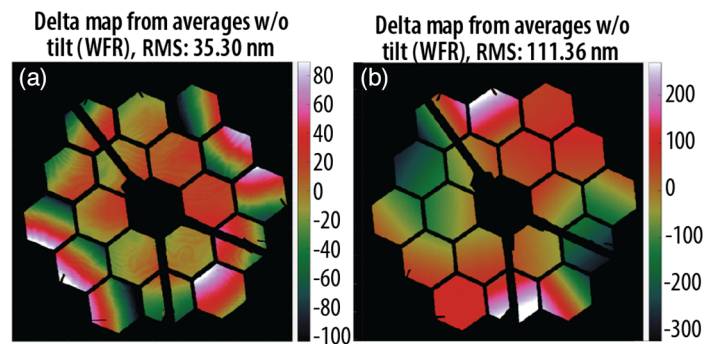


**Fig. 17** Thermal stability WFE measurements from JSC cryogenic tests revealed unexpected drifts, attributed to the CoCOA (a) and IEC thermal cycling (b).

#### 4.4.4 Thermal distortion stability anomalies and problem resolution

Two unexpected optical instabilities in the WFE of the PM, which ultimately were traced to thermo-mechanical effects, were observed during the OTIS cryovacuum test. These two errors were correlated (1) to the act of carrying out interferometry measurements of the PM with the CoCOA and (2) to cycling of the IEC heaters. WFE maps that are characteristic of these two types of instability are shown below in Fig. 17. The root causes of these instabilities and the associated mitigations are discussed in the following sections.

*Primary mirror long term drift instability (CoCOA-measurement and frill-induced).* During the OTIS optical testing, an unexpected longterm PM WFE drift,  $\sim 350$  nm of PM WFE over 6 h, was observed when the CoCOA shutter was opened. This assembly housed the center-of-curvature interferometer used to measure the PM during the test. When the shutter opened at cryogenic conditions, it would heat the telescope. Review of thermal telemetry revealed that sensors on thermal blankets that are part of the PM frill (a stray light mitigation feature) and PMSA thermal close-outs (COs) showed a temporal response with a similar time constant to the WFE transient.

The frill is a series of single-layer insulation (SLI) blankets attached to brackets that were fastened to interfaces on the primary backplane support structure (PMBSS) to which the mirrors were attached. The blankets were tied and taped to the aluminum brackets and then tied and taped to one another. The PMSA edge COs are a series of blankets that closed out the edges of mirror segments along their outer perimeter, attaching to the frill brackets and normal to the frill. The frill and edge COs are shown in Fig. 18.

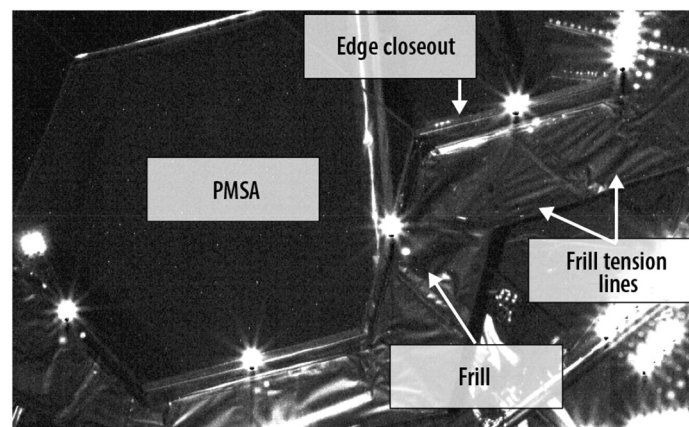


**Fig. 18** PG image showing frill tension lines that indicate the intended slack in the blanketing was not achieved. Temperature variations with a taut frill induced forces into the PM support structure and caused unanticipated temperature-dependent wavefront drifts.

The SLI blankets were chosen as a low mass alternative to a composite structure made from the same materials as the PMBSS. It also provided a soft structure that was more resilient to damage and enabled tailoring late in the design flow for areas of uncertainty, e.g., the overlap in the frill between the wings and center section, and the clearance for the sunshield bipods. With the decision to use SLI instead of a composite frill came the potential for thermal-distortion-induced errors, and the potential for thermal stability challenges. The frill brackets being structural was included in the thermal distortion and dynamics models of the system. The loads imparted to the telescope structure from cooldown were assessed and included in the stability predictions. The requirement for the frill SLI to be slack on-orbit at cryogenic temperatures and thus not exert any load on the support brackets was flowed to the design of the blankets.

Nevertheless, the most probable root cause for PM long term drift was determined to be the frill and PMSA COs becoming taut during cooldown; and then applying time-varying loads directly into the PMBSS as the frill and edge COs changed temperature in response to the CoCOA shutter opening and closing. This root cause was confirmed by review of *in-situ* images, direct inspections at ambient temperatures, modeling of the test conditions, and ultimately on-orbit performance after re-work.

Images captured with the cryogenic PG system were reviewed, and what appeared to be tension lines were observed in blankets on the +V2 and -V2 wings. A reference image is shown in Fig. 18. To prove that tension occurred in the system, inspections of the blanket slack were made following the test. This was accomplished by applying a normal force to the edge of the seam between adjacent blankets in two directions to determine the range of free out-of-plane motion of the frill, and thus (by calculation) the linear slack in the SLI between brackets. For each edge CO, the slack was measured directly by manually shifting the CO in each direction and measuring how far it could be moved before being stopped by the string ties. The required slack for each blanket was determined using the material properties, CTE, worst-case cool down, and the blanket dimensions. When the measurements were compared to the worst-case cool down predictions, multiple locations were found to have insufficient slack, and these locations correlated to where tension lines were seen in the PG images. An example of the inspection is shown in Fig. 19.

The structural model of the telescope was used to simulate the effects of tension release caused by the CoCOA shutter opening and heating the system. Equal and opposite forces were applied to adjacent frill brackets in the structural model, simulating the reduction of tension loads in the blankets that spanned between the brackets as the frill and COs warmed. The resultant WFE for these loads were calculated using the model, which determined that on average a change in tension of 1 N could yield on the order of 20 nm of WFE. An example of this modeling analysis is shown in Fig. 20. This confirmed that the frill blankets could be the source of the WFE observed during the test. The types of mirror displacements modeled were comparable to what was measured.

Post-test inspections found that there were implementation issues that prevented the frill and edge CO from providing the required slack. The implementation of the frill, and the requirement to not load the structure, was intended to be verified by design, and with qualitative inspections. The design was not reviewed with the same processes used for structures and mechanisms, allowing it to be improperly implemented without quantitative inspections that would have identified the problem during installation.



**Fig. 19** Frill blanket inspection measured the slack when a force was applied normal to the edge of the seam between adjacent blankets. This inspection method confirmed that many locations did not have the designed slack.

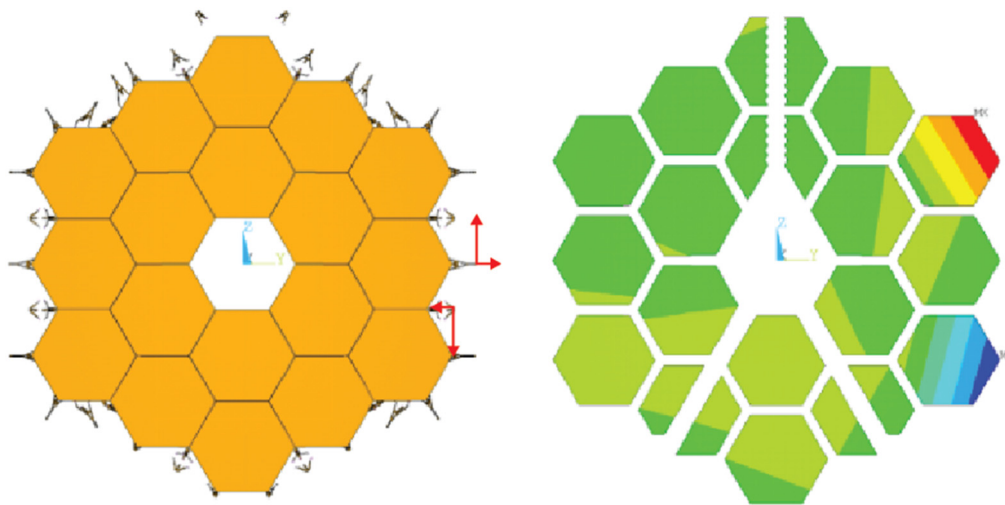


**Fig. 20** Frill tension modeling (left) with red arrows showing where the forces were applied. The resultant WFE map is shown at right, confirming that frill tension can cause similar WFE to what was observed in test.

The corrective action was to rework the frill and CO where feasible to increase slack. The model developed to aid in root cause determination was used to guide the rework process and to predict the eventual on-orbit stability contribution from this effect, which was predicted to be acceptable for the reworked hardware. This rework required re-tying all of the splices between adjacent blankets and designing new parts to enable the amount of slack in the blankets to be tailored. Slack inspections were performed for each set of blankets using the worst-case cool-down requirements. When the slack was insufficient, the seams and ties of the blankets were adjusted to generate sufficient slack. Additional qualitative inspections were performed due to limitations of the inspection method, including looking for signs of tension in the blankets during the slack measurement in other directions. These inspections, combined with the modeling of the system, were used to justify not repeating the complex cryogenic-vacuum test. The inspections carried out demonstrated that the various blankets on the OTE had sufficient slack. This conclusion was confirmed on-orbit, where the thermal stability performance of JWST exceeds requirements and the predicted performance.

A key lesson learned was the importance of defining quantitative and qualitative inspections that properly interrogate the system including soft structure. When design requirements are identified, the proper inspection methods and workmanship details need to be defined. In highly sensitive systems, there is the potential to need more inspections to validate workmanship and system behavior. Defining prescriptive inspections is critical, as is understanding the limitations of an inspection. Included in the inspections were the images from the PG system taken at temperature. These were a key diagnostic tool. The value of imagery and/or video, during assembly, integration, and test should not be understated. In this case, and for many others on JWST, it was critical to support troubleshooting.

**Cyclic optical instability (IEC heater-induced oscillations).** The second unexpected instability seen during OTIS optical testing was a cyclic drift observed in both PM center-of-curvature interferometry (WFE on the order of 100 nm) and SI pass-and-a-half imaging data. Review of thermal telemetry revealed that the time varying behavior of the WFE and LOS response correlated with changes in the IEC radiator panel temperatures. Testing determined that oscillatory (cyclic) radiator temperature changes resulting from “dead band cycling” associated with the thermal control approach led to cyclic WFE drift on the order of 50 nm per K of temperature change. Tests showed that decreasing the magnitude of the radiator panel temperature change (by reducing the heater control deadband) correspondingly decreased the magnitude of the WFE oscillations. Additionally, bulk radiator temperature changes resulting from set point temperature changes were shown to lead to WFE drift. This issue was observed at cryogenic conditions, and, fortunately, was reproducible during ambient operations, enabling

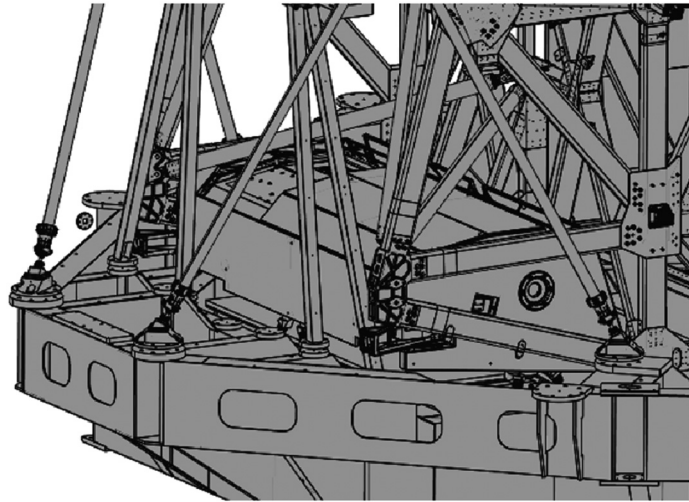


**Fig. 21** Warm IEC in the test configuration at JSC (center structure inside the struts) showing the complex mechanical interfaces.

troubleshooting operations and inspections to directly detect and/or test for it after the completion of the cryogenic vacuum test.

A detailed error tree was constructed to evaluate the problem and define the root cause. Given that the WFE change was correlated to heater operation and was reproducible, the most likely root cause was that a mechanical interface, or short, between the IEC and telescope was causing the problem.

The IEC is connected to the telescope through a harness tray on the deployable tower assembly (DTA) and through the harness on that tray, the harnesses that connect it to the ISIM, and thermal insulation. The harness tray, while mechanical in nature, was hinged, with gaps at the hinges designed to accommodate relative motion of the IEC to the rest of the telescope. In addition to these connections there were a number of critical clearances between the IEC and OTE. These interfaces, both flight and ground test critical clearances, and ground-test-specific interfaces were inspected to identify both mechanical and thermal shorts. The non-flight interfaces to the IEC were primarily thermal insulation and temperature sensors, with one significant exception, the six struts that supported the IEC during the test. An image of the IEC in the JSC test configuration is shown in Fig. 21.

On-orbit the IEC is designed to be isolated from the rest of the telescope by attaching it with three flexures. These flexures were not sufficient to support the IEC in a 1-G ground test configuration, so it was supported on rigid struts. During nominal ground operations and launch, the IEC was secured with three launch lock mechanisms. The only time the IEC was not supported through the launch interfaces was for the JSC cryogenic vacuum test. The struts were designed to maintain the alignment of the IEC to the telescope within specific tolerances from ambient to cryogenic conditions and back.

As part of the root cause evaluation, it was identified that the IEC support condition was approximately 100 times stiffer than the on-orbit configuration, and thus an unintended stiff interface between the IEC and the telescope could cause load to be applied to the telescope structure that may result in WFE. The IEC applying loads into the PMBSS through harness “mechanical shorts” driven by radiator panel temperature changes and reacted by a non-flight-like structural support was determined to be the most probable root cause for the cyclic drift.

In the thermal test chamber, the IEC and telescope were inspected for mechanical and thermal shorts. These included clearance checks, thermal insulation inspections, checks of the IEC harness tray to verify it was working properly (e.g., the hinges were not bound), and inspections of the harnesses to verify they were behaving as expected. These inspections found that the planned mechanical interfaces behaved as expected, but that there were unplanned contacts between the IEC thermal insulation and the telescope structure, which could be an issue in flight. These contacts were categorized as “soft” as inspection tools built from Kapton and other soft materials could be passed between the interfaces with light hand applied force. Beyond that no

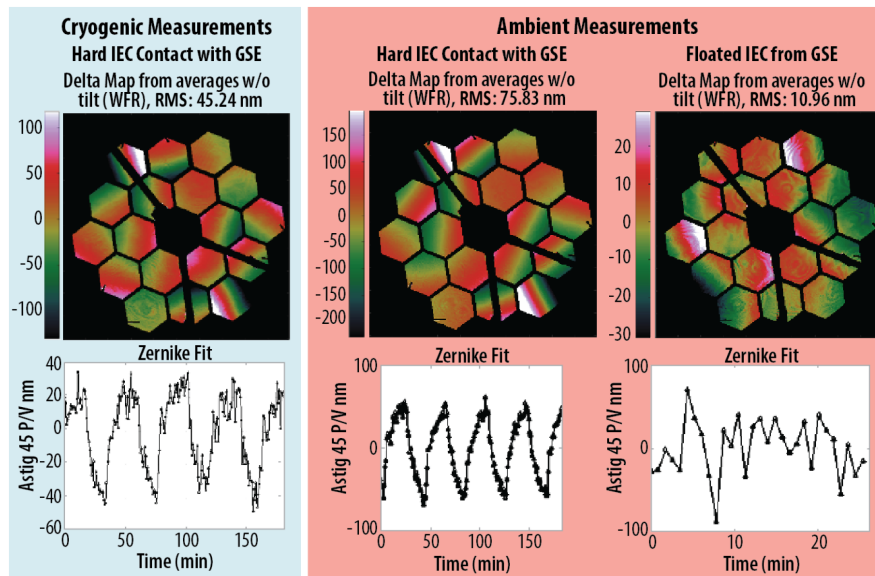


**Fig. 22** In ground test, IEC WFE thermal oscillation measurements were observed at both cryogenic temperatures and at ambient temperatures. When the IEC was floated from the ground support equipment (GSE), the observed drift was considerably mitigated. This indicated there was a mechanical short with the ground support equipment contributing to the effect, a contribution that would not be present in flight. Nevertheless, there was still a small flight contribution from the IEC harness cable (see Fig. 26).

other mechanical shorts could be found. These interferences were determined to not be significant thermal shorts but were improved after the fact to the extent possible and several follow-up inspections tracked them carefully through ground processing.

Offline testing was performed to determine the stiffness of the harness connecting the IEC to the telescope. The stiffness data were then used to model a mechanical short between the IEC and telescope, and this model accurately predicted the cyclic instability observed during the test. This model was used to predict the on-orbit stability contribution from this effect, incorporating the validated mechanical short model and utilizing the flight IEC support condition, which was predicted to be acceptable.

The modeling and inspections clearly determined that this was the most probable root cause, but could not prove this was the root cause. To prove that the on-orbit performance would be sufficient, a test was designed to “float” the IEC relative to the telescope in a more flight-like manner. The exact boundary conditions could not be met, but similar boundary conditions could be achieved by offloading the IEC at ambient conditions, and connecting it to the telescope with flexures. Modeling of the system predicted that this approach would reduce the observed WFE by an order of magnitude. Measurements performed during the cryogenic vacuum test, after the test at ambient conditions, and after the IEC was “floated” are shown below in Fig. 22. These images are shown along with time-variant Zernike fits for IEC thermal cycling. The cryogenic and ambient measurements show a similar shape that correlates to the IEC heaters being cycled. That shape is not present in the floated configuration, and the error term shows significant reductions, as expected. This test demonstrated that the ground test configuration was the primary root cause, and that even if the mechanical interferences found during the inspections were present on-orbit that the effect would be significantly less than seen during the test.

As an additional mitigation for flight, the radiator panel temperature control “dead band” was reduced from  $\pm 1.0^{\circ}\text{C}$  to  $\pm 0.25^{\circ}\text{C}$ . Further reductions in the deadband were found not to be useful, given the granularity of the relevant temperature sensor telemetry and the complex interactions of the heaters on the separate but not fully decoupled IEC radiator panels.

The IEC thermal cycling issue is illustrative of how deviations from “test as you fly” place a greater burden on the evaluation of ground tests. It also demonstrated that in extremely sensitive systems, components that are usually treated as negligible can have significant effects. Harness stiffness measurements, and the use of that stiffness data in models is more common in

deployable systems and not standard practice in static systems. The same is true for other soft structures, such as SLI and multi-layer insulation (MLI). If the harness had been included in the thermal distortion model, the ground test configuration would have identified this as a potential problem, and that may have resulted in a change to the test configuration, added inspections and requirements on the flight hardware, and a better prediction of the expected test WFE. Finally, this shows the criticality of testing. Had a “hard” mechanical short been present in the system, it may not have been detected by other testing, and it would have significantly impacted on-orbit performance. Meanwhile the efforts to diagnose what was primarily a ground configuration issue led to the determination that cable stiffnesses themselves did impart some forces even on-orbit when floating and this realization allowed the team to reduce the deadband on the ground by a factor of 4 and further splay harnesses as much as possible. It turned out that this factor of 4 reduction in deadband was critical as this effect is actually the largest contributor to thermal stability on orbit over typical observation times.

**Hub thermal shield assembly.** Similar to the frill there was an issue with the blankets that provided the thermal COs between the telescope and the SC and sunshield. A potential interference was found, and during this inspection, it was determined that the blankets may not have had sufficient slack to account for the total relative motion between the telescope and SC. In the deployed state, the telescope is connected to the SC through harnesses, the cryocooler line, the star tracker assembly, (4×) 1-Hz isolators, and the hub thermal shield assembly (HTSA) blankets. The HTSA blankets are shown in Fig. 23 and they connect the DTA to the SC and Sunshield to help isolate heat from the SC from the cold side of the observatory. The intent of this design was to limit dynamic disturbances from the SC from resulting in optical disturbances on the telescope.

Unlike with the IEC, specific testing and analysis had been performed on the harness configuration, and the star tracker assembly, to enable proper on-orbit predictions and define the requisite ground inspections. The blankets that formed the HTSA had a similar design requirement to the frill with the function to provide slack. Unfortunately, this requirement was not fully quantified nor was clear inspection criteria provided. The HTSA was made up of three blankets, two of which were 0.005” thick Kapton (layers 1 and 2), and the third was made of MLI (layer 3). Using lessons learned from the frill, inspections were made of the upper layer, and the MLI layer that confirmed the slack was insufficient to meet the needs of the mission. Like the frill, this was attributable to qualitative inspections being used.

The lower layers, which also had previously been inspected for slack, when formed to the shape required by the thermal design and fully installed, had created a rigid interface between the telescope and SC. After the layer, three inspections determined that re-work was required to achieve the required slack, additional review and inspections of layers 1 and 2 were performed. Access limitations and a lack of explanation as to the intent of the slack resulted in this escape during the initial inspections.

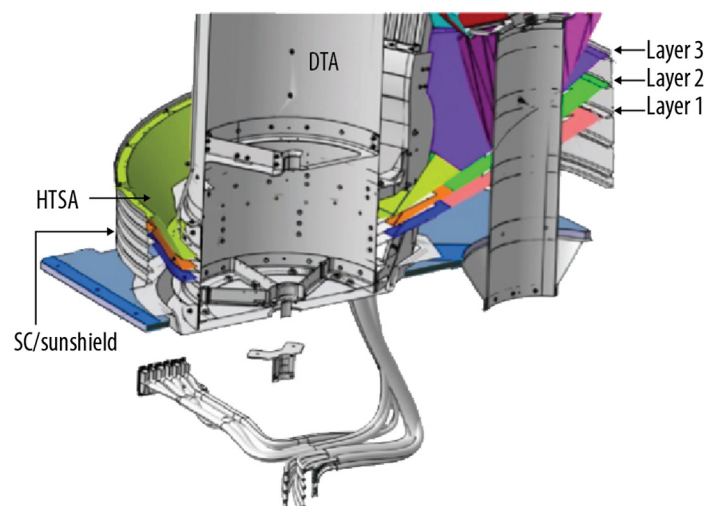


**Fig. 23** HTSA blankets provided critical COs in the core area to isolate the SC from telescope.

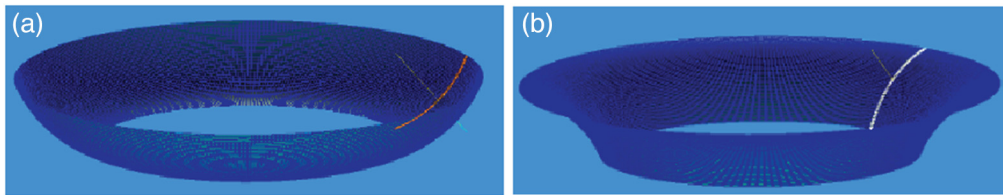


**Fig. 24** HTSA blanket modeling of the radial slack with the cone wall curved in (a) and out (b).

A mockup of this interface was rapidly constructed to validate that the baseline design would yield an undesired rigid system. Analysis of the design using inspection data and evaluating different shapes to bind all possible outcomes after launch and deployment of the telescope confirmed this potential rigidity. Figure 24 shows two of the shapes analyzed. That analysis found that the blankets had a stiffness that ranged from similar levels to the nominal mechanical interfaces to orders of magnitude greater. If the interface had been left in place as originally implemented, it could have introduced tens to hundreds of nanometers of WFE into the system.

Thermal modeling based on test data was used to show that the lower blankets, layers 1 and 2, were not required to meet mission requirements. These layers were ultimately eliminated from the design. The MLI upper layer blanket was re-built to enable slack, and detailed inspections were performed at multiple points to confirm that slack. The blanket was then closed out to the SC with a new thermal gasket that was designed to eliminate potential problems found in the baseline design and exacerbated by the additional slack. On-orbit, there has been no evidence of a mechanical short or thermal leak at this interface, validating that the workmanship and inspections performed were satisfactory.

The lessons learned from the HTSA blanket situation are extremely similar to the frill and IEC, with the additional lesson that mockups and understanding the physical nature of the hardware is critical. A simple mockup of the 0.005" thick SLI secured in a conical shape quickly demonstrated the problem. In addition, the modeling and testing of the harness and star tracker assembly demonstrated that with proper attention to detail and understanding of the physical system issues can be avoided.

## 4.5 On-Orbit Results/Comparison to Predictions

### 4.5.1 Pointing stability drift (star tracker to OTE boresight)

Pointing stability following slews can arise due to the different locations of the star tracker on the hot SC side of the observatory and the FGS on the cold telescope side. Relative star tracker and FGS LOS drifts due to thermal changes will cause inter-boresight motion that produces a guide star offset in FGS in the V2/V3 plane, which will be corrected through the ACS loop with offset loops and FGS to SC coordinate system updates. However, the rotational drift about the V1 axis is not sensed by the ACS system and not corrected. Cross correlation of wavefront weak lens data produced extremely small radial and translational drifts, as shown in Fig. 25, well below the allocation of 1.8 milliarcseconds.<sup>5</sup>

### 4.5.2 ISIM electronics compartment cyclic drifts

As part of the thermal stability monitoring of the observatory, the IEC cyclic drifts discussed in section cyclic optical instability (IEC heater-induced oscillations) were evaluated during commissioning. This was done by staring at a bright star with a weak lens and performing phase retrieval on images taken every eight seconds to measure the wavefront cyclic drift. The wavefront was then decomposed into Zernike coefficients and those were correlated against thermal sensors in the IEC that were shown to be related to the wavefront change during JSC testing. As discussed, the deadband itself had been reduced to only  $\pm 0.25$  K (originally  $\pm 1$  K) so the expectation was that the resulting wavefront variations would be small. The data shown in Fig. 26 below indicate that the oscillations were in fact very close to predictions. The wavefront change is primarily focus and astigmatism (single component model mixes focus and astigmatism), at a level in line with the peak of 3.5 nm RMS predicted from the OTIS cryo-vacuum test (average is 0.8 nm RMS).

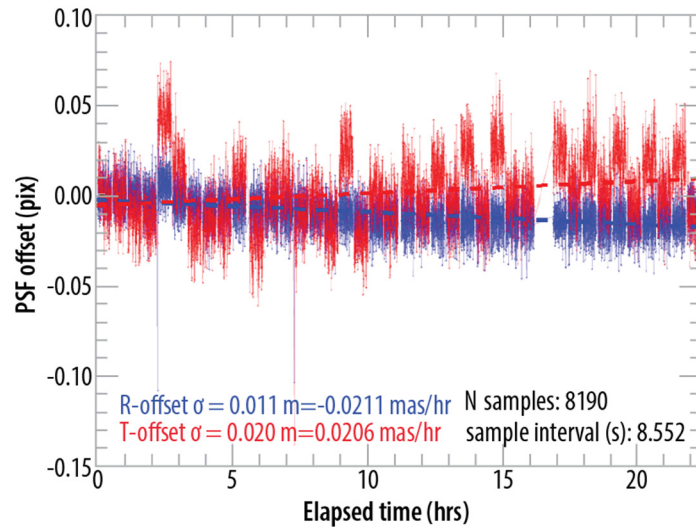


**Fig. 25** Relative star tracker and FGS thermal drifts will cause inter-boresight motion that produces a guide star offset in FGS in the V2/V3 plane, which will be corrected through the ACS loop, and rotational drift about the V1 axis. The rotational drift is not sensed by the ACS system and not corrected. The on-orbit inter-boresight drift between guider and NIRCcam after a large thermal slew is shown to be well below the prediction of 0.79 mas/hr.

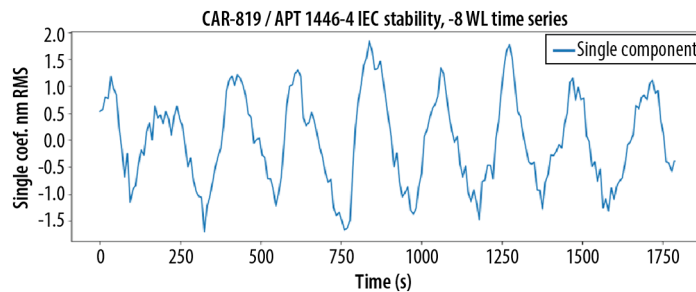


**Fig. 26** IEC wavefront in nanometer RMS with  $-8$  waves weak lens and a single coefficient.

In addition to just measuring the overall wavefront, a few key thermal sensors on IEC instrument panels that have heaters were shown to be correlated to the wavefront oscillations. This analysis used influence functions derived from ground testing with the temperature sensors and compared against the wavefront measured by phase retrieval every eight seconds. Figure 27 shows the measured and modeled IEC WFE drifts as a function of time. The associated fitting error of the process was 0.25 nm RMS of a total signal of 0.8 nm RMS and 70% of the variation was explained through the correlation of just three sensors and associated heater panels.

#### 4.5.3 Frill and thermal distortion

A telescope stability test was carried out in order to evaluate the performance of the telescope over days following a large slew designed to provide a worst case change in temperature. The test included stabilization and measurement, slew, and then measurements over time to evaluate how a large change in the thermal environment would impact the telescope stability. The expectation was that this test would evaluate the magnitude and time constant associated with the frill and would evaluate the longer timescale backplane time constant. The results from this test are shown in Figs. 28 and 29, with the results tabulated in Table 3. The frill magnitude and the backplane magnitude were very close to the integrated modeling predictions. However, the time constants associated with the frill and backplane drifts were faster than models predicted. The thermal transient models were not validated as it was not considered a performance requirement though validating transient models might be needed for future missions that require knowledge of time dependent changes.

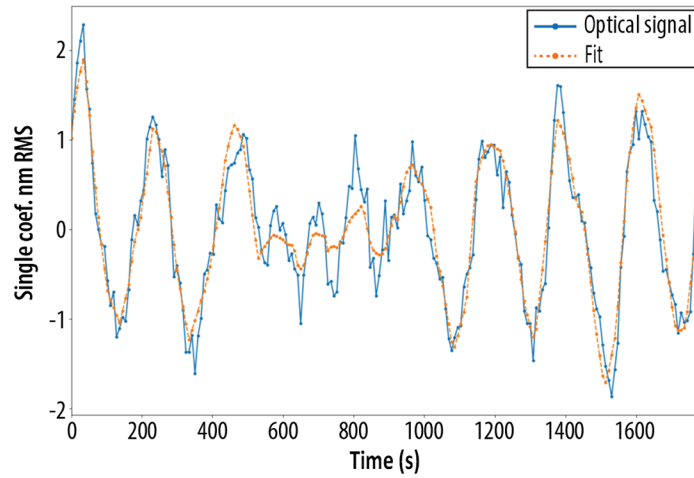


**Fig. 27** Comparison of predicted wavefront from IEC thermal sensor telemetry to actual wavefront drift.

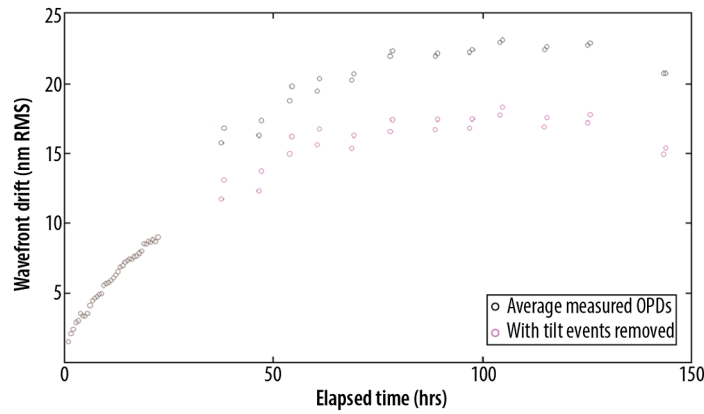


**Fig. 28** Telescope thermal stability measured during the on-orbit thermal stability test showed a total wavefront drift in line with integrated modeling predictions. The tilt events needed to be removed from the drift measurements, as tilt events are spontaneous mechanical events unrelated to the temperature drifts.

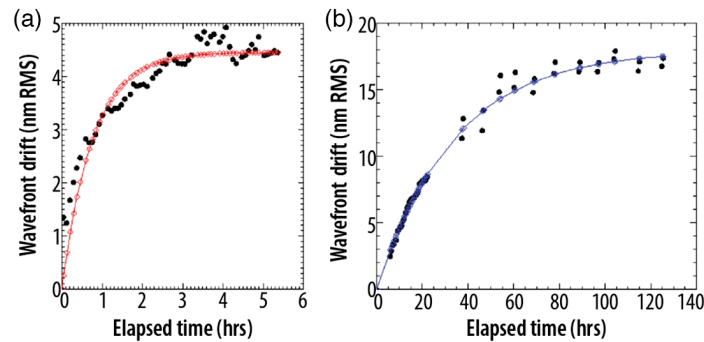


**Fig. 29** Frill CO distortion (a) and OTE thermal distortion (b), with data plotted in black circles and exponential fits plotted with colored diamonds. Both datasets are on-orbit data from the thermal stability activity.

**Table 3** Stability performance predicted by integrated modeling and as measured in flight. The predicted values reported are for the beginning of life properties.

| Contributor        | Predicted amplitude (WFE nm RMS) | Measured amplitude (WFE nm RMS) | Predicted response              | Measured response        |
|--------------------|----------------------------------|---------------------------------|---------------------------------|--------------------------|
| IEC heater cycling | 3.5                              | 2.5                             | 240 to 480 s period oscillation | 224 s period oscillation |
| Frill and PMSA CO  | 9                                | 4.45 ± 0.19                     | 8 to 10 h time constant         | 0.77 h time constant     |
| Thermal distortion | 14.4                             | 17.94 ± 0.39                    | 5 to 6 day time constant        | 1.41 day time constant   |

## 5 Tilt Events

### 5.1 Ground Testing

Tilt events are sudden, unplanned tilts of one or more PM segments. Segment piston generally accompanies these tilts but was more difficult to cleanly measure during ground testing, so we refer to these only as “tilt events” and did not typically determine segment piston as well. In flight, increased measurement precision allows all piston, tip, and tilt to be measured, and corrected.

During cryogenic testing of the telescope (OTE) at the Johnson Space Center, measurements with the Multi-Wavelength Interferometer revealed the occurrence of tilt events. The interferometer was located at the PM center of curvature above the vertically oriented telescope. An early test with only two segments present (OGSE1) revealed a tilt event of about 8 microradian WFE magnitude (physical segment tilt would be half of this level) and alerted the team to search for similar events in the later, comprehensive OTE test (July to October 2017). During the flight OTIS cryovacuum test (see Sec. 4.4.1), frequent measurements of the reflected wavefront from the entire PM were made using the center of curvature interferometer throughout testing as part of the planned test procedures and to monitor for any tilt events. Analysis of the tilt events were made and cross checked by different analysis teams.

Tilt events occurred as two types: the majority were single segment tilts, whereas fewer featured correlated tilts over multiple segments. Measured tilts were typically several micro-radians WFE. The sensitivity limit of measurements was estimated to be about 1 micro-radian. For reference, a single segment tilt of 1 micro-radian imparts about 80 nm RMS over the entire PM. At NIRCcam, this size tilt would create a single segment image displaced about 6.5 pixels from the nominal image with about 1/18 energy of the total image and a size about 5× that of the nominal PSF. Rephasing had been expected to be needed about every 14 days to correct for potential wavefront drift; more frequent rephasing due to tilt events would reduce observing efficiency.

The cause of tilt events may be the relieving of residual stress in the telescope backplane composite structure and joints, or interfaces with this structure, caused by the change from room to cryo temperatures. This was not a smooth, continuous process but rather expressed itself as small “lurches” of the segments. As stress is relieved, the frequency and magnitude of the tilt events would be expected to decline, as was observed throughout the course of the ground OTIS cryo-vacuum testing. Indeed, over the final, thermal stabilization testing only a few candidate events were observed and plausible causes for each were determined. That is, it was not clear that any true, tilt events occurred through this stable period. While the frequency of several microradian scale events was low by the end of the test, it was possible that smaller events were occurring below our detection limit and might still be seen in-flight.

### 5.2 Flight Tilt Events

From the ground testing experience, there was awareness of the possibility of tilt events during flight. The primary means of flight detection was by the nominal WFE sensing procedure using the NIRCcam weak lenses to perform phase retrieval of the end-to-end telescope and NIRCcam optical path. These measurements have been performed roughly every 2 days following initial

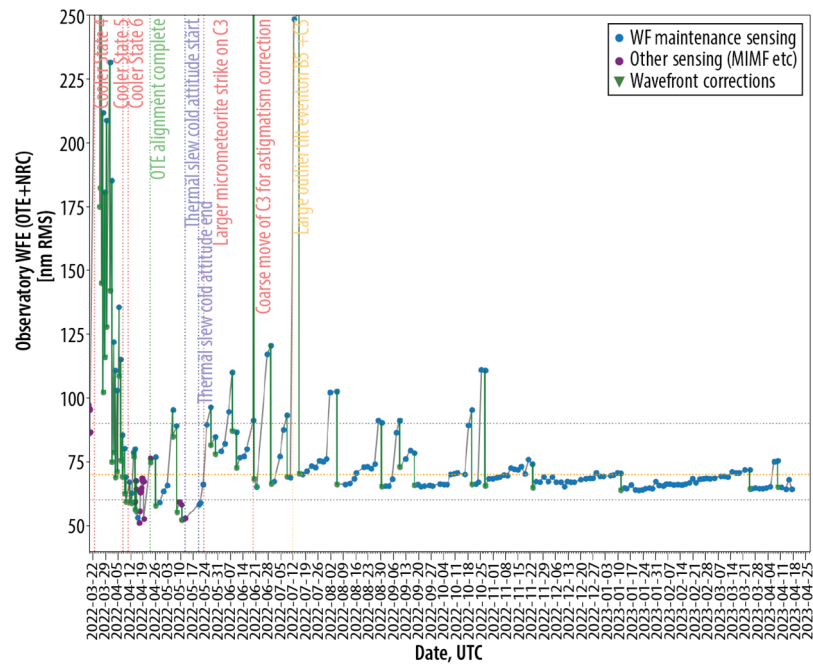


**Fig. 30** Trending plot of the observatory (telescope + NIRC) WFE determined by the nominal monitoring procedure at a 2-day cadence. Tilt events are evident as WFE jumps from the nominal baseline of about 70 nm RMS to levels around 100 nm RMS (plus one large event in July 2022). By the end of May 2022, tilt events were the dominant source of instability; however, their frequency has declined so much that they are now rare events with much smaller magnitudes (figure courtesy of the STScI JWST WFS&C team).

telescope phasing. Telescope phasing was completed on April 23, 2022, and routine wavefront monitoring commenced.

Figure 30 tracks the measurements of observatory (telescope + NIRC) RMS WFE following initial phasing. By May 2022, during science instrument commissioning, the dominant source of WFE instability, which required wavefront correction was the occurrence of tilt events. Tilt events are indicated in the figure as abrupt changes of observatory WFE to a level of up to about 100 nm RMS from a stable base value of about 70 nm RMS. After each of these events, the corrective control returned the tilted segment to its nominal alignment, reestablishing the baseline WFE level. Only one very large event was detected on July 12, which briefly raised the WFE to about 240 nm prior to correction, attributed to an anomalously large micrometeoroid impact. The larger tilt events tend to involve correlated motions of all three segments on a given OTE wing, consistent with stick/slip release of stress at the PMBSS hinge interface. The frequency of the typical, smaller events has been decreasing with time, as seen in the figure. By the end of October 2022, the tilt event frequency had declined so much and the observatory stability was very good that telescope maintenance is now needed less frequently than the originally expected 2-week cadence. As of May 2023, tilt events continue to occur, most often as individual segment events with amplitudes <15 nm RMS, occasionally as high as 30 to 50 nm. Over the first nine months of Cycle 1, the telescope required corrections roughly once per month, including for the correction of the gradual accumulation of these small tilt events. Tilt events will continue to be tracked and corrected as necessary but it appears they have become infrequent and are unlikely to cause a significant impact to observations or observatory efficiency.

### 5.3 Tilt Event Lessons Learned

At this point, the tilt event story is mostly a cautionary tale for future missions. We believe these events are likely due to discontinuous stress relief throughout the backplane structure, including composite parts and joints, as well as the wing hinge interfaces for some events, driven primarily by the large cooldown transition. While we expected them, we did not have models predicting

the magnitude or frequency of these events and characterized them during testing of completed structures. The decline of magnitude and frequency of events we measured during testing was expected to continue during flight but the time scale for this was not known.

A key question is how relevant the JWST experience is for future missions. Though we have measurements of tilt magnitude and frequency over time for JWST, this is likely specific for the JWST design, construction, and cryogenic operating temperatures. A program of materials testing including joint assemblies and other interfaces would provide insight into this effect especially for HWO operating at nearly room temperature with fine thermal control. It could be that maintaining a constant temperature alone reduces these types of release events, but HWO will be sensitive to even finer levels and at near-room-temperature operations desorption will be a contributor. The overall architecture though will need to be considered as an actively controlled segmented telescope can sense and control tilt events and so testing will mainly help with bounding the dynamic range and frequency of this type of approach.

The key lesson learned from the tilt events is that future missions should be aware of instabilities with similar composite structures and wing latch interfaces. The JWST pre-planned, 2-day cadence of wavefront sensing enables correction of tilt events in a timely manner, and permitted commissioning activities to proceed with little impact from these events. The 6-month commissioning period provided sufficient time for JWST system stabilization while tilt events declined to a level where they have had no significant effect on science observations.

## 6 Lessons Learned for the Future Great Observatories

The development of JWST was challenging for many reasons<sup>16</sup> but meeting stability requirements for an observatory this large, lightweight, and cryogenic was one of the top challenges. Given the size, the complexity of the design and the environment JWST could not apply NASA's standard verification process of "test-as-you-fly." Its stability had to be verified solely by analysis, the novel processes of which were successfully demonstrated on JWST, standardizing the methodologies to future Astrophysics missions. There are many lessons learned presented herein but the following top level lessons learned can be derived and applied to future great observatories to improve on the verification process demonstrated on JWST:

1. Reliance on model validation alone is not sufficient for understanding stability. Models are typically a representation of the as-designed configuration from CAD models, whereas tests may uncover deviations in the as-built hardware due to workmanship. The latter can only be evaluated by inspection and/or test. Workmanship testing and/or inspection of the as-built configuration is important for stability and should be treated with the same rigor as wavefront or alignment tests, including the development of verification or crosscheck matrices. Identifying workmanship issues is facilitated by performing pre-test analyses of the flight hardware in the test configuration and in the test environment to quickly identify deviations from the as-designed predictions above the allowed uncertainties.
2. Soft structure is highly prone to workmanship issues and can become taut with temperature or can move with venting and requires special levels of inspection, audits, and workmanship testing where it influences performance.
3. An auxiliary of lessons (1) and (2) is that sufficient schedule slack needs to be planned to retrofit workmanship issues identified during the tests. For those workmanship issues that can not be corrected satisfactorily, enough margin must be available in the error budgets to cover the unexpected error contributors.
4. The integrated modeling approach of using worse-case analysis assumptions in combination with MUFs proved to have bounded the on-orbit performance and provided margin for unknowns such as workmanship issues, micrometeoroids and end-of-life degradations. In particular, the approach for structural dynamics jitter analyses was generally conservative and can be revisited using the JWST on-orbit performance as a basis.
5. Heater operation can structurally deform systems affecting stability through secondary load paths such as harnesses and should be tested as part of workmanship verification.
6. Mockups and careful attention to detail should be used to evaluate soft structure effects on stability and associated inspection requirements and processes required.

7. Verification test considerations during as early as the architecture phase is critical. Verifying stability is challenging and subject to workmanship, but an approach that makes maximum use of active controls can provide a simpler verification strategy, one in which even workmanship surprises can be mitigated. In addition, the architecture should minimize the risk of workmanship from soft structures by isolating them from the stability path or making them highly inspectable. Early design trades on architectures and technologies should consider the ability to verify an architecture.
8. Most of the soft structure surprises on JWST could have been avoided through alternative designs or by better inspections, but the complexity of soft structure makes it difficult to anticipate every possible workmanship issue and argues to avoid it architecturally when possible and to add workmanship testing when it cannot be avoided.

---

### Code and Data Availability

The JWST integrated model simulations and ground test data are not made publicly available as they are restricted by International Traffic in Arms Regulations (ITAR) and Export Administration Regulations (EAR). The on-orbit flight data from Secs. 4.5 and 5 is publicly available through the MAST archive (see <https://mast.stsci.edu/>).

### Acknowledgments

The efforts to design, build, measure, and in some cases address issues with JWST stability included a huge team from NASA, industry, and academia. Many of the testing and trouble-shooting efforts required huge personal sacrifice. We cannot recognize everyone who contributed to these efforts in this paper, but the success of JWST and the lessons learned summarized in this paper are the results of their hard work and attention to detail. Elements of the study were carried out at the JPL, California Institute of Technology, under a contract with the National Aeronautics and Space Administration (Grant No. 80NMO018D0004). The data that support the findings of this article are available in the JWST MAST Archive, and the analyses performed use a variety of commercial and private codes. Where applicable, they can be requested from the author at [Lee.D.Feinberg@nasa.gov](mailto:Lee.D.Feinberg@nasa.gov).

### References

1. M. W. McElwain et al., “The James Webb Space Telescope mission: optical telescope element design, development, and performance,” *Publ. Astron. Soc. Pac.* **135**, 058001 (2023).
2. L. D. Feinberg et al., “Commissioning the James Webb Space Telescope optical telescope element,” *Proc. SPIE* **12180**, 121800T (2022).
3. P. A. Lightsey, A. A. Barto, and J. Contreras, “Optical performance for the James Webb Space Telescope,” *Proc. SPIE* **5487**, 825 (2004).
4. M. B. Vila et al., “JWST cryo fine guidance closed loop test results,” *Proc. SPIE* **10698**, 106983R (2018).
5. G. Hartig and M. D. Lallo, “JWST Line-of-Sight Jitter Measurement during commissioning,” Tech. rep. JWST-STScI-008271, Space Telescope Science Institute. [https://www.stsci.edu/files/live/sites/www/files/home/jwst/documentation/technical-documents/\\_documents/JWST-STScI-008271.pdf](https://www.stsci.edu/files/live/sites/www/files/home/jwst/documentation/technical-documents/_documents/JWST-STScI-008271.pdf).
6. J. Arenberg et al., “The JWST backplane stability test article: a critical technology demonstration,” *Proc. SPIE* **6265**, 62650Q (2006).
7. P. B. Karlmann et al., “Continued development of a precision cryogenic dilatometer for the James Webb Space Telescope,” *Proc. SPIE* **5528**, 63 (2004).
8. L. A. Riddle, J. R. Tucker, and A. Marcel Bluth, “Composite tube and plate manufacturing repeatability as determined by precision measurements of thermal strain,” *Proc. SPIE* **8837**, 212–218 (2013).
9. B. Saif et al., “Measurement of large cryogenic structures using a spatially phase-shifted digital speckle pattern interferometer,” *Appl. Opt.* **47**, 737 (2008).
10. R. A. Kimble et al., “James Webb Space Telescope (JWST) optical telescope element and integrated science instrument module (OTIS) cryogenic test program and results,” *Proc. SPIE* **10698**, 1069805 (2018).
11. J. B. Hadaway et al., “Performance of the center-of-curvature optical assembly during cryogenic testing of the James Webb Space Telescope,” *Proc. SPIE* **10698**, 1069803 (2018).
12. K. Yang et al., “Thermal model performance for the James Webb Space Telescope OTIS cryo-vacuum test,” in *48th Int. Conf. on Environ. Syst.*, Albuquerque, New Mexico, ICES-2018-35 (2018).
13. L. D. Feinberg et al., “James Webb Space Telescope system cryogenic optical test plans,” *Proc. SPIE* **8150**, 815007 (2011).

14. C. Wells et al., “Primary mirror segment assembly integration and alignment for the James Webb Space Telescope,” *Proc. SPIE* **7793**, 779309 (2010)
15. S. R. Lunt et al., “Use of close range photogrammetry in James Webb Space Telescope alignment testing under cryogenic conditions,” *J. Astron. Telesc. Instrum. Syst.* **6**, 018005 (2020).
16. L. Feinberg et al., “Breaking the cost curve: applying lessons learned from the James Webb space telescope development,” *Proc. SPIE* **10698**, 1069823 (2018).

**Lee D. Feinberg** is the JWST Telescope Manager and optics lead for JWST at the Goddard Space Flight Center. He received a BS degree in optics from the University of Rochester and an MS degree in applied physics from John Hopkins University. He is the author or coauthor of well over 100 papers on space telescopes and optics. He is an SPIE Fellow and a GSFC Senior Fellow.

**Michael W. McElwain** is the JWST Observatory Project Scientist. He is a senior research astrophysicist at the NASA Goddard Space Flight Center, where he is in the Exoplanets and Stellar Astrophysics Laboratory. His research interests include large space telescopes and specialized instrumentation for exoplanet characterization with direct imaging, transit spectroscopy, and radial velocities. He earned his PhD at the University of California, Los Angeles, where he was a member of the Infrared Laboratory. He was a postdoctoral researcher at Princeton University and a science and technology policy fellow at the National Academies before joining NASA Goddard.

Biographies of the other authors are not available.